Miguel Soares Maranha Tiago

UNTETHERED BATTERY-FREE BIO-MONITORING STICKERS USING FAR FIELD ENERGY HARVESTING

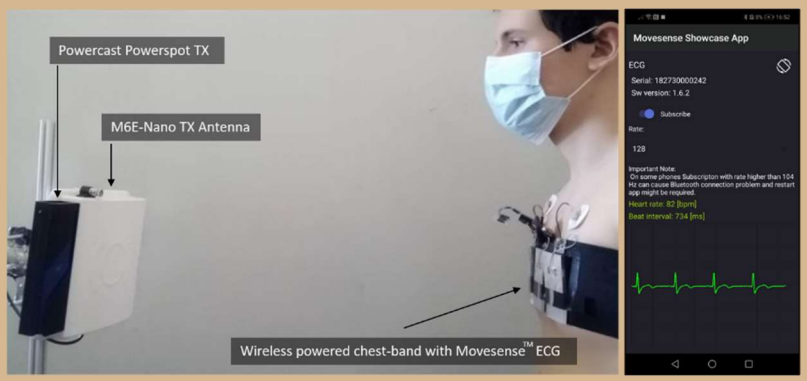

Dissertação no âmbito do Mestrado Integrado em Engenharia Electrotécnica e de Computadores orientada pelo Professor Doutor Mahmoud Tavakoli e apresentada ao Departamento de Engenharia Electrotécnica e de Computadores.

Outubro de 2020

University of Coimbra

Faculty of Sciences and Technology

Department of Electrical and Computer Engineering

Untethered Batteryfree Biomonitoring Stickers Using Far Field Energy Harvesting

Miguel Soares Maranha Tiago

A dissertation presented for the degree of

Master of Science in Electrical and Computer Engineering

Coimbra, 2020

1 2 9 0

FACULDADE DE CIÊNCIAS E TECNOLOGIA
UNIVERSIDADE D COIMBRA

Untethered Batteryfree Biomonitoring Stickers Using Far Field Energy Harvesting

Supervisor:

Prof. Doutor Mahmoud Tavakoli

Jury:

Prof. Dr. André Manuel dos Santos Mendes

Prof. Dr. David Emanuel Dias

Prof. Dr. Mahmoud Tavakoli

A dissertation submitted in partial satisfaction of the requirements for the degree of Master of Science in Electrical and Computer Engineering

Coimbra, 2020

This work was performed in collaboration with the project "Add.Additive" (Reference Nr. 59563), co-financed by the European Regional Development Fund (ERDF), through the "Programa Operacional Competitividade e Internacionalizacão" (POCI-01-0247-FEDER-024533). Funding also came from the CMU-Portugal project WoW (45913) which had support of European Regional Development Fund (ERDF) and the Portuguese State through Portugal2020 and COMPETE 2020, and the project "Dermotronics" (Reference: 31784), funded by "Fundos Europeus Estruturais e de Investimento" (FEEI), through the "Programa Operacional Regional do Centro".

Acknowledgments

First of all, I would like to thank Prof. Doctor Mahmoud Tavakoli of the Electrical and Computer Engineering Department of the Faculty of Science and Technology at University of Coimbra, for his help and guidance. He was always available when I needed, not only during the research phase, but also during writing. It was a pleasure to be a part of his team and witness his vast knowledge and experience. I eagerly awaited the weekly team meetings, there was always something new and interesting to learn from my fellow colleagues. I must also thank them for their help and for teaching me how to use the laboratory equipment.

To my parents, Pedro and Susana who have always loved me, supported me, and gave me everything I needed to reach this point. To my sister Maria João, that was always there for me when I needed it, to family's unconditional support over the years. To my girlfriend who was by my side during this journey and my friends who have been with me the whole time.

Abstract

In the last few years, wearable bioelectronics received an increasing interest due to their applications in Internet of Medical Things (IoMT), digital healthcare, and domiciliary hospitalization. Among those, soft and stretchable bioelectronics patches are interesting, as they can lead to ultrathin, imperceptible, comfortable, and skin-conformable systems for long-term patient monitoring. However, as any other mobile devices, the main limiting factor is the power source, which is even a bigger problem for soft electronics that hold the promise to reduce the number of mechanically rigid components that are used in these systems. For this reason, Wireless Power Transfer (WPT) has been of interest for recharging and even supplying continuous power to these types of devices. In this dissertation we study the feasibility of using the far-field energy harvesting, in order to continuously power biomonitoring patches. The ultimate goal is to reach a point where electrophysiological data from the human body can be acquired and wirelessly transmitted, using fully passive, untherthered, and batteryless patches, that interface with the human skin. To do so, we designed, optimized, fabricated and characterized a series of wearable Radio Frequency (RF) WPT antennas, including printed, soft, and stretchable antennas and compared their performance against design parameters, the substrate material, the conductive material, distance from the harvester, etc. After several evolutionary designs, we obtained an optimal printed antenna design that is less sensitive to the body proximity, and provides a promising energy harvesting of $0.0825 mW/cm^2$ at a 30 cm distance. We then show that by occupying $20 cm^2$ of a wearable chest-band with an antenna, this system can be used to power an Electrocardiogram (ECG) measurement device at a distance of 55 cm. The overall results are satisfactory, and hold the promise for fulfilling the fully wireless biomonitoring patches in near future.

Keywords: Wearable applications; Biomonitoring; Far field; Wireless power

transfer (WPT), Radio Frequency Identification (RFID);

Resumo

Nos últimos anos, os dispositivos bioeletrónicos vestíveis têm suscitado bastante interesse, devido às suas vastas aplicações, como na internet médica das coisas, na saúde digital, e na hospitalização domiciliar. Entre eles, os adesivos eletrónicos flexíveis e elásticos são interessantes, pois podem levar a sistemas ultrafinos, confortáveis, impercetíveis e que se adaptam à pele, que efetuem monitorização a longo prazo do paciente. No entanto, como qualquer outro dispositivo móvel, o principal fator limitante é a fonte de energia, o que é um problema ainda maior para os dispositivos eletrónicos flexíveis que prometem redução do número de componentes mecanicamente rígidos usados nesses sistemas. Por este motivo, a transferência de energia sem fios é uma possível solução para recarregar e até mesmo fornecer energia contínua para esses tipos de dispositivos.

Nesta dissertação estudámos a viabilidade de usar a transmissão de energia pelo campo distante, a fim de alimentar continuamente os adesivos eletrónicos de biomonitorização. O objetivo final é chegar a um ponto onde os dados eletrofisiológicos do corpo humano possam ser adquiridos e transmitidos por tecnologia sem fios, usando adesivos eletrónicos totalmente passivos, desconectados e sem bateria, que fazem interface com a epiderme humana. Para tal, foram desenhadas, otimizadas, fabricadas e caracterizadas uma série de antenas para transferência de energia por radiofrequência, incluindo antenas impressas, flexíveis e extensíveis. Foram comparados os desempenhos de cada antena com as suas dimensões, substratos, material condutor, distância ao transmissor de radiofrequência, etc. Após vários designs evolutivos, obtivemos um desenho da antena otimizado que é menos sensível à proximidade com o corpo humano, e fornece uma captação de energia promissora de $0.0825 mW/cm^2$ a uma distância de 30 cm. De seguida, mostramos que, usando este Sistema numa faixa peitoral vestível de $20 cm^2$, é possível alimentar um dispositivo

de medição de eletrocardiograma a uma distância de 55 cm. Os resultados em geral são satisfatórios e mantêm a promessa de cumprir os adesivos de biomonitorização totalmente sem fios num futuro próximo.

Palavras-chave: Dispositivos vestíveis; Biomonitorização; Campo distante; Transferência de energia sem fios; Identificação por radiofrequência;

Contents

Acknowledgments **i**

Abstract **iii**

Resumo **v**

List of Acronyms **xi**

List of Figures **xvi**

List of Tables **xvii**

1 Introduction **1**

1.1 Motivation and Objectives 4

1.2 Outline of the dissertation 6

2 State of the Art **7**

2.1 Wireless Power Transfer 7

2.1.1 Near-Field wireless power transfer 10

2.1.2 Far-Field wireless power transfer 11

2.2 Printed and Stretched Electronics 16

2.3 Work Focus 20

3 Far-Field Energy Harvesting **21**

3.1 Radio frequency harvesting: Operation method 21

3.2 System Characterization 23

3.2.1 Transmitter module 23

3.2.2 Harvester module 25

3.2.3 RF harvester classification 26
3.2.4 Chapter Summary 29

4 Antenna Design and Optimization **31**
4.1 Antenna fabrication using flexible materials 31
4.1.1 Antenna evaluation 33
4.1.2 Antenna geometry and multi-materials 37
4.2 Planar Inverted-F Antenna 42
4.2.1 PIFA Modeling and Simulation 43
4.2.2 Chapter Summary 51

5 Case studies **53**
5.1 PIFA Experimental results 53
5.2 Feasibility results and application 60
5.2.1 ECG acquisition device. 60
5.2.2 WPT Biomonitoring prototype 62
5.2.3 Chapter Summary 64

6 Conclusion **67**
6.1 Future work 68

Bibliography **76**

Appendices **77**

A Python code to configure the RFID Reader **79**

B RF Harvester fabrication **81**
B.1 RF Harvester Circuit Schematics 81
B.2 RF Harvester Circuit Fabrication 82

List of Acronyms

AC Alternating Current

Ag Silver

ANT Adaptive Network Topology

API Application Programming Interface

BLE Bluetooth Low Energy

BP Blood Pressure

BT Bluetooth

CMOS Complementary Metal Oxide Semiconductor

Cu Copper

dB Decibel

dBi Decibel Isotropic

dBm Decibel Miliwatt

DC Direct Current

DUT Device Under Test

ECG Electrocardiogram

EDA Electrodermal Activity

EEG Electroencephalogram

EGaIn Eutectic Gallium Indium

EMG Electromyogram

ESA Electrically Small Antennas

HHESA Helix-Based Hemispherical ESA

HR Heart Rate

HTTP Hypertext Transfer Protocol

IBD Implantable Biomedical Device

IoMT Internet of Medical Things

IoT Internet of Things

LED Light Emitting Diode

LM Liquid Metal

LoS Lab on Skin

MCU Microcontroller Unit

MEMS Micro-Electro-Mechanical System

MRC Magnetic Resonance Coupling

NFC Near Field Communication

PCB Printed Circuit Board

PDMS Polydimethylsiloxane

PEIRP Peak Effective Isotropic Radiated Power

PIFA Planar Inverted-F Antenna

PTE Power transmission efficiency

REST Representational State Transfer

RF Radio Frequency

RFID Radio Frequency Identification

RR Respiration Rate

Rx Receiver

SAR Specific Absorption Rate

SIS Styrene-isoprene block copolymers

SoC System on Chip

SpO_2 Arterial Oxygen Saturation

TPU Thermoplastic Polyurethane

Tx Transmitter

UHF Ultra High Frequency

VNA Vector Network Analyzer

VSWR Voltage Standing Wave Ratio

WBAN Wireless Body Area Networks

WPT Wireless Power Transfer

List of Figures

1.1 Applications of IBD and LoS devices. 2
1.2 2019 Market snapshot of the printed, organic and flexible electronics industry. 3
1.3 Possible scenario for a WPT system. 4

2.1 Wireless power transfer mechanism for a batteryless capsule endoscopy system. 8
2.2 A few wirelessly powered implants. 10
2.3 Antenna Simulation with anatomical human body(Duke model) . . . 12
2.4 Examples of implantable biomedical devices powered by RF antennas. 13
2.5 Examples of RFID applications. 14
2.6 Body area network with soft sensor nodes. 14
2.7 Body area network with soft sensor nodes. 15
2.8 Photo of a flexible microstrip patch antenna composed of liquid metal, encased in PDMS. 16
2.9 Wireless, battery-free system for vital signs monitoring in neonatal intensive care. 17
2.10 Miniaturized microstrip patch antenna prototype and measurement setup. 18
2.11 Stretchable antenna designs using different materials. 19

3.1 RF Harvesting system diagram. 22
3.2 Picture of the SparkFun M6e-Nano UHF RFID Reader. 23
3.3 Picture of the UHF RFID antenna. 24
3.4 Picture of the Powercast PowerSpot TX91503. 24
3.5 Powercast P1110B energy harvesting device. 25

3.6 Assortment of Powercast antennas. 26
3.7 Schematic of the RF harvester classification method. 26
3.8 Harvested power over distance for the Powercast 6.1 dBi antenna. . . 27
3.9 Harvested power over distance for the Powercast 1 dBi antenna. . . . 27
3.10 Schematic of the 2-Stage Dickson charge pump. 28
3.11 Fabricated RF to DC harvester. 28

4.1 Fabricated flexible version of the Powercast 1 dBi omnidirectional antenna. 32
4.2 Schematic of the 1 dBi flexible antenna fabrication process. 33
4.3 Visual interpretation of the S-parameters for a two port network. . . 34
4.4 S_{11} parameters for the rigid and flexible 1 dBi antenna. 35
4.5 Measured capacitor voltage at the harvester output. Comparison between the rigid PCB antenna and the flexible antenna. 36
4.6 Folded dipole antenna layout and design parameters. 37
4.7 Pictures of the fabricated folded dipole antennas, using different materials. 38
4.9 Folded dipole WPT experiment setup. 40
4.10 Folded dipole WPT stretchable sticker. 40
4.11 Basic PIFA design. 42
4.12 PIFA Antenna layout and design parameters. 43
4.13 PIFA on the phantom model, in the simulation environment. 44
4.14 Fabricated Casula2019 PIFA characteristics. 45
4.15 Simulation results for varying PDMS ($\varepsilon_r = 2.67$,$tan\ \delta = 0.37$) substrate height. 46
4.16 Simulation results for varying distance to the human body phantom. . 46
4.17 Proposed PIFA optimized layout, and design parameters comparison with Casula2019 PIFA design. 47
4.18 Proposed PIFA characteristics. **a)** Top view and size comparison with Casula2019 PIFA. **b)** Measured and simulated S_{11} of the fabricated antenna. 47
4.19 Size comparison between the Casula2019 PIFA and the proposed PIFA. **a)** Top view. **b)** Side view. 48

4.20 Proposed PIFA simulated radiation pattern. **a)** 3D Model. **b)** 3D Radiation Pattern. **c)** Azimuth plane pattern. **d)** Elevation plane pattern. 49
4.21 Schematic of the stretchable conductive layer fabrication process. . . 50
4.22 Stretchable proposed PIFA fabrication process. 50
4.23 Stretchable proposed Ag ink PIFA. **a)** Top view. **b)** Measured and simulated S_{11} of the fabricated antenna. 51
4.24 Stretchable proposed Ag PIFA being deformed. 51

5.1 Experiment setup. Antenna is placed at a fixed distance, **a)** on free space, **b)** on a subject chest. 53
5.2 RF Harvester supercapacitor charge time, comparison between free space and on body placement of the Casula2019 PIFA. Experiment was done with the antenna at a fixed distance of 30 cm from the Tx. 54
5.3 RF Harvester supercapacitor charge time, comparison between Casula2019 and the proposed PIFA. Data was acquired with both antennas at 30 cm from the Tx, on a human subject body. 55
5.4 Supercapacitor charge time comparison between Casula2019 PIFA, the proposed Cu PIFA and the stretchable Ag conductive ink PIFA. Data was acquired with both antennas at 30 cm from the Tx, on free space. 56
5.5 Dual RF transmitter experimental setup. 56
5.6 Supercapacitor charge time while using each RF transmitters individually, and both at the same time. Data was acquired with the antenna at 30 cm from the Tx, on free space. 57
5.7 Triple RF harvester configuration. 58
5.8 Comparison between, a single RF harvester with the proposed PIFA and three RF harvesters in parallel with proposed PIFAs. Data was acquired with all antennas at 30 cm, on free space. 58
5.9 Supercapacitor charge time comparison between the triple array placed on body and on free space at 30 cm . The data was acquired while using two RF Tx. 59

5.10 Total amount of power harvested over distance, while using three harvesters with three proposed Cu PIFAs, using two RF Txs. 59
5.11 Movesense wearable sensor platform by Suunto. 60
5.12 Prototype WPT chest-band with ECG device. 62
5.13 Application of the prototype WPT chest-band. 63
5.14 Case study, chest-band output voltage while monitoring ECG on a subject. 64

List of Tables

2.1 Maximum Human Exposure to Radio Frequency Electromagnetic Fields. 9

3.1 JADAK Thingmagic M6e-Nano UHF RFID reader specifications. . . 23
3.2 External UHF RFID antenna specifications. 24
3.3 Powercast TX91503 transmitter specifications. 25
3.4 Output power of the P1110B harvester for the 330 Ω load resistor . . 29

4.1 Correlation of VSWR and reflected power. 35
Folded dipole antenna design parameters 37
4.2 Fabricated folded dipole antennas specifications and measured values. 41
Casula2019 PIFA design parameters. 43
Design parameters comparisson between Casula2019 PIFA and ours proposed PIFA. 47

5.1 Summarized VNA measurements for the three fabricated PIFAs detailed in section 4.2.1. 54
5.2 Measured power consumption of the Movesense^{TM} device. 61
5.3 Harvested power over distance, on free space and on human body, for the triple harvester configuration, using two Txs. 65

Chapter 1

Introduction

Electrophysiological monitoring consists in the acquisition, processing and communication of surface biopotentials in the surface of human skin. This data can contains important information about human physiology, such as muscular, heart, and brain activities[1]. Wearable devices for biomonitoring such signals are used in sports,[2] health monitoring[3] and human-machine interfaces.[4] Remote health monitoring, based on non-invasive and wearable sensors, actuators and modern communication and information technologies offers an efficient and cost-effective solution to reduce expensive healthcare facilities, allowing remote patient monitoring[3].

Wearable sensors are a category of biomonitoring systems, that are intended for long-term monitoring of various electrophysiological data, including Electrocardiogram (ECG), Electromyogram (EMG), Heart Rate (HR), Electrodermal Activity (EDA), Blood Pressure (BP), Arterial Oxygen Saturation (SpO_2), Respiration Rate (RR) and body temperature[5]. Several studies also focus on using these data for early detection and diagnosis of various health problems, including cardiovascular[6], neurological and pulmonary diseases[7]. Usually the data acquired by the sensors are transmitted to a nearby node using a communication protocol, that should consume the least amount of power possible, like ZigBee,[8] Bluetooth (BT),[1, 9] Near Field Communication (NFC),[10, 11] and Radio Frequency Identification (RFID).[12]

Till this date, Implantable Biomedical Device (IBD) and Lab on Skin (LoS) devices have mostly relied on rigid batteries for their operation. Although batteries are the most reliable source of energy existing today for reliable operation, they are bulky and rigid. There exist a large mechanical mismatch between the soft hu-

man organs and traditional rigid electronics. During the last decades, many groups worked on printed, soft and stretchable thin film to address this problem. Despite the successful implementations, one problem has remained unsolved. Energy supply. Current systems rely on rigid batteries, which despite being reliable, are not soft, and have limited time of operation.

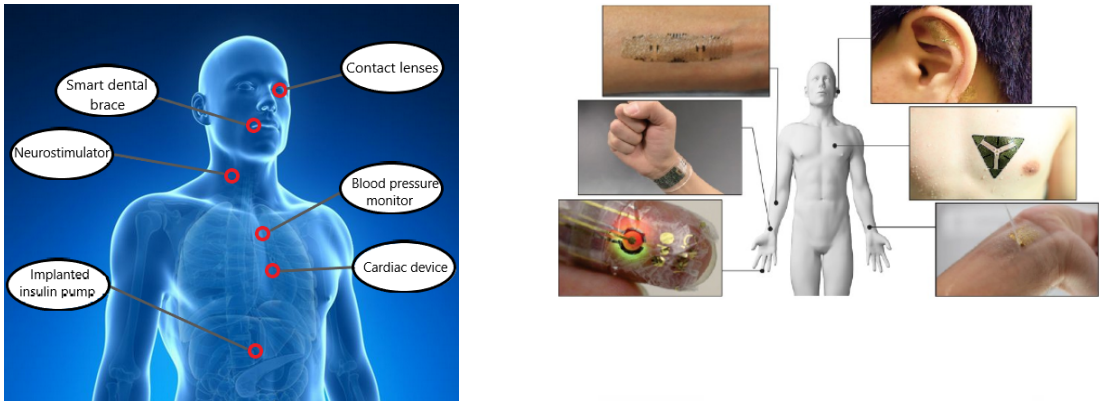

Figure 1.1: Applications of IBD(left) and LoS devices(right), from [13].

Till now, various sources for energy harvesting for biomedical systems have been investigated. This includes electrochemical energy harvesting through vibration, mechanical energy harvesting through piezoelectric systems, photovoltaic through solar cells, thermoelectric through temperature differences, inductive, Radio Frequency (RF) and ultrasound[14].

Power harvesting has been a heavily researched topic, due to the possibilities of extending the life of biomedical devices by recharging the battery, or even completely remove it, enabling the miniaturization of these devices and thus increasing their usability. Among those, RF harvesters are very attractive, due to their versatility, as they are not dependent to external factors such as light, mechanical movement, and temperature gradient.

This work studies utilization of printed and stretchable RFID antennas for application in wearable biomonitoring patches. If successful, RFID antennas can be printed in biomonitoring patches that embed other sensing devices, and electronics interconnects, with the ultimate goal of fully wireless, and batteryless monitoring of patients electrophysiological data. These types of devices are wearable patches containing soft, flexible, and stretchable electronic devices, which comfortably contact

with the epidermis to deliver a range of functionalities[13]. This paradigm was introduced in 2011 to bridge the gap between the flat and rigid wafer-based conventional technologies and the soft curvilinear surfaces of biological tissues[15].

With the development of new technology, the applications wearable biomonitoring devices are being significantly expanded, the wearable market alone is approximately evaluated at 16.12 billion in 2020 with a compound annual growth rate (CAGR) of 22.37% facing last year.

The total RFID market is worth $11.6 Billion in 2019, expected to rise to $13 Billion in 2022. This includes tags, readers and software/services for RFID labels, cards, fobs and all other form factors, for both passive and active RFID[16].

The total market for printed, flexible and organic electronics will grow from $41.2 Billion in 2020 to $74 billion in 2030 according to IDTechEx. The key market components are depicted in Figure 1.2, where the printed and flexible sensors represent $3.9 Billions in 2019[17].

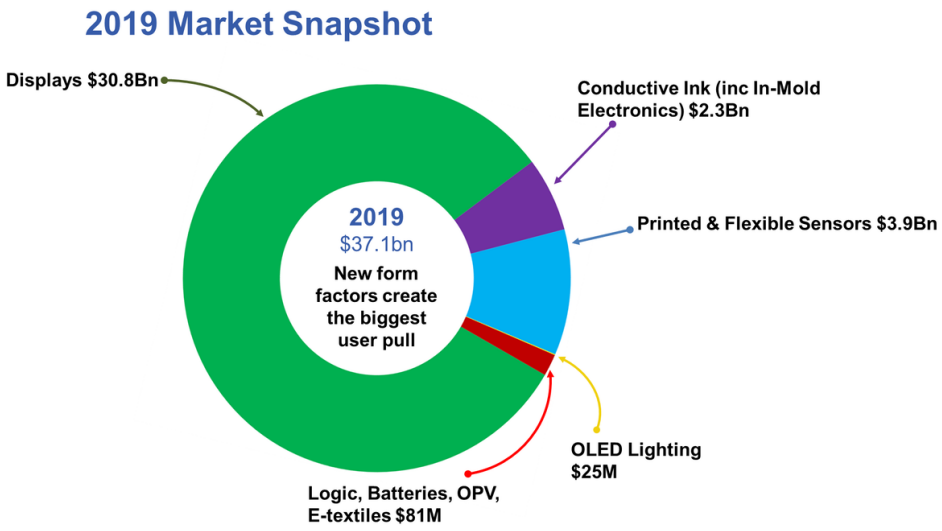

Figure 1.2: 2019 Market snapshot of the printed, organic and flexible electronics industry.

1.1 Motivation and Objectives

Wireless Power Transfer (WPT) is becoming increasingly important for wearable biomonitoring, and Internet of Medical Things (IoMT) systems that perform continuous health monitoring. Soft and stretchable bioelectronics patches are a promising solution for patient monitoring, due to their physical properties of being skin-conformable and comfortable. A primary challenge of these epidermal patches is power supply. Batteries are large, bulk, and are associated with high mechanical modulus. WPT can be a solution for this problem, by providing energy wirelessly to directly power the device.

In this work the feasibility of removing the battery of LoS biomonitoring device will be evaluated. One possible way of reducing the overall size of these devices, is by making the battery obsolete[14]. Near-field power transfer systems offer only a limited operating distance, as opposed to far-field energy transfer, that can provide continuous power transfer to the device over a few meters, therefore making the battery redundant, and the system possibly less bulky.

A possible scenario for a epidermal biomonitoring application using far-field WPT, can be observed in Figure 1.3, where the patients could move around the hospital room with hassle-free wireless monitoring, such Electronic skin (e-skin) patches adhere to the human epidermis to collect physiological and behavioral data. This can be used to identify physiological and emotional responses through the collection and classification of diverse multimodal data, including heart, muscle and brain activities (ECG/EMG/EEG respectively).

Figure 1.3: Possible scenario for WPT system. From[18].

The main goal of this dissertation is to study printed and stretchable RFID antennas for application in unthethered and battery-free biomonitoring patches. To do so, several research questions should be studied and answered.

- How the efficiency of the printed and stretchable RF antennas compares with traditional rigid circuit board antennas?
- How the geometry of the antennas and the materials (i.e. dielectric substrate), affect the efficiency of the RF antennas, in terms of harvested energy;
- How is RF antenna performance affected when in close contact with the human body?
- Can we obtain heart rate and full ECG waveform without a battery, using this antenna, and what should be the footprint of the RF antenna to afford the required amount of the energy for this case.
- How the distance between the transmitter and antenna affects the harvested energy?

For the purpose of answering these questions, we started by fabricating several stretchable antennas using different dielectric substrates and designs. An efficiently working antenna is required to harvest the maximum possible amount of energy from the electromagnetic waves, therefore this work aims to design and print a stretchable soft RFID antenna that is minimally affected by the human body, but still efficient enough to provide maximum power transfer. This stretchable antenna is going to be connected to a RF/DC energy harvester to convert the RF energy into Direct Current (DC), and thus providing the required energy to power a biomonitoring application, such as an ECG device with a power consumption of around 5 mW.

The printed antennas will be characterized in terms of their Voltage Standing Wave Ratio (VSWR) and center frequency, using a Vector Network Analyzer (VNA). Once the results are satisfactory and ensure device operation, we will study an application of the optimized printed antennas to power a biomonitoring patch, to send a full ECG wave. The ECG wave is selected as compared to other physiological data such as temperature monitoring, or heart rate monitoring, it is considerable more energy demanding. It should be noted that RF can be used as well for data

communication, which makes it potentially very interesting system for simultaneous wireless data and energy transmission. However the focus of this dissertation is only energy harvesting through RF systems, and for data communication we rely on Bluetooth Low Energy (BLE).

1.2 Outline of the dissertation

This thesis is organized in 6 chapters. The first is an introduction to the theme of this dissertation, discussing some of the main motivations and objectives.

In chapter 2, the state of the art is presented. Initially, a concise history of Wireless Power Transfer (WPT) is presented with the health hazard regulations of electric and magnetic fields. Following that, a brief overview of near field WPT is analyzed, and after that, a more in depth analysis is given, regarding related work on far-field WPT for biomedical applications and stretchable electronics.

Chapter 3 presents the working principles of RF energy harvesting, alongside the used technologies, such as, the RF wireless power transfer device, stock antennas, and the harvesting system. Then a classification of the harvesting system is conducted, using the supplied rigid antennas.

Chapter 4 presents the developed work in the antenna design and optimization. The evaluation criteria of antenna parameters will be discussed, as well as essential materials and methods for fabrication. Afterwards, antenna fabrication process using multi-materials and computer simulated models are examined.

In Chapter 5, the case studies and experimental results of the selected antenna design for the harvesting system are analyzed and discussed. Both rigid and stretchable versions of the antenna are compared in regard of total harvested power. Following that, different configurations of the harvesting system are studied and validated trough a biomonitoring chest band prototype.

Finally in chapter 6, the final conclusions from the present work will be laid out together with future work for the proposed WPT system.

Chapter 2

State of the Art

In the following chapte,r the state of the art of WPT and printed and stretched electronics for wearable biomonitoring are discussed. A brief history about each section is given, as well as an overview about the technologies and applications. The WPT section is divided in two parts: near-field and far-field. On the far-field only RF energy transfer is detailed, taking into account the context of the dissertation.

2.1 Wireless Power Transfer

WPT is the transmission of electrical energy without wires between devices this type of transmission is categorized has three different types: electromagnetic induction, Magnetic Resonance Coupling (MRC) and RF reception[19].

Wireless power and data transfer dates of the 19^{th} century. James C. Maxwell had predicted the existence of radio waves in 1864 and in 1888, Heinrich Hertz's experiments verified the predicted propagation of electromagnetic waves and its properties, using a spark gap oscillator, dipole antennas and parabolic reflectors [20]. Nikola Tesla devoted nearly fifty years to developing his ideas of wireless transmission. In 1891 he made a breakthrough, and invented the high frequency and high voltage transformer known as "The Tesla Coil". Nikola Tesla demonstrated the first wireless power transfer by means of electrostatic induction using a high-tension induction coil before the American Institute of Electrical Engineers at Columbia College.

During the the early 1970's WPT through biological tissue was demonstrated.[21] High levels of power (ranging from 50 W to 1 kW) were transmitted though inductive coupling, where a coil was surgically implanted at a depth of about 7.5mm in the chest of a dog. The electromagnetic response of biological tissue imposes a serious reduction on the power and integrity of RF waves. The human body can reflect and absorb this waves, introducing attenuation delay and phase distortion of the RF signals. Thus it's considered a harsh environment for propagation of RF fields[14].

An example of a WPT device for biomedical application is shown in Figure 2.1. The system relies in three major components; the first one is the end-fire helix power transmitter under floor that consists of a DC source and a DC/AC converter which enables the WPT at the intended frequency. The second component of the circuit is the open-ends helix located in the patient's jacket that acts as a power repeater. And the third component is the loose-coupling with a small size receiving antenna inside the capsule, this small device employs an AC/DC converter with a DC/DC converter (regulator). In this way the endoscopic capsule receives the required energy to move inside the internal body organs.

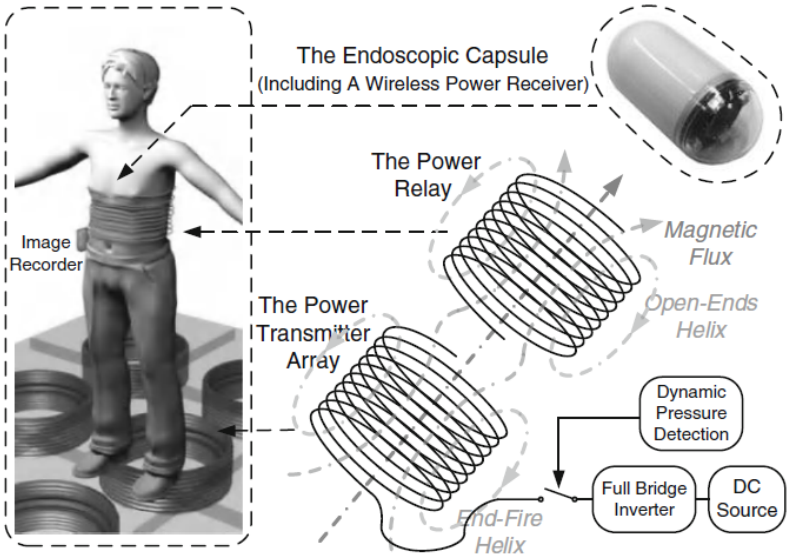

Figure 2.1: Wireless power transfer mechanism for a batteryless capsule endoscopy system [22].

Health Risk Limits

Health risks should be addressed when designing WPT systems, the human body absorbs some of the energy and it may cause heating in surrounding tissues. These type of systems follow guidelines and regulations, which limit electromagnetic exposure, to ensure human safety. The amount of energy absorbed by a body exposed to an electromagnetic field is measured using Specific Absorption Rate (SAR). It is defined as the power absorbed per mass of the tissue, with units of W/kg or mW/g [23].

In order to prevent harmful effects and regulate the usage of frequency bands the International Commission on Non-Ionizing Radiation Protection (ICNIRP) and the IEEE C95.1-1991 standard regulates the electric and magnetic fields strength limits for public use for the frequency range between 3 kHz-300 GHz, as stated in Table 2.1. For frequencies between 10 MHz and 10 GHz, the SAR must be below 0.08 W/kg, averaged over a 6 minute period[24]. For an average adult human weighing about 80 kg, the 6 minute average absorption must be under 6.4 W.

Frequency Range (MHz)	**Electric Field Strength , (E) (V/m)**	**Magnetic Field Strength, (H) (A/m)**	**Power Density (S) E-Field, H-Field ($\mathbf{mW/cm^2}$)**	**Averaging Time $\|E\|^2$,$\|H\|^2$ (minutes)**
0.003-0.1	614	163	100, 1 000 000	6
0.1-3.0	614	16.3/f	100, 10 000/f^2	6
3-30	1842/f	16.3/f	900/f^2, 10 000/f^2	6
30-100	61.4	16.3/f	1, 10 000/f^2	6
100-300	61.4	0.163	1	6
300-3 000	-	-	f/300	6
3 000-15 000	-	-	10	6
15 000-300 000	-	-	10	616 000/$f^{1.2}$

Table 2.1: Maximum permissible exposure for humans to radio frequency electromagnetic fields[25].

2.1.1 Near-Field wireless power transfer

Near-field WPT is now ubiquitous with wireless chargeable smart devices, ranging from every day devices to medical, such as smartphones, smartwatches, Internet of Things (IoT) devices, electric cars and IBDs. Before inductive power transfer became popular amongst wearable gadgets and IoT devices, it had been one of the most successfully deployed wireless powering techniques used in transdermic implants, such as cochlea[1]prosthetics.

In 1998, T. Akin et al. [26] were pioneers in the presentation of an implantable neural recording system powered and controlled using a 2 MHz RF telemetry link. This system recorded signals from axons and transmitted them to the outside world. In recent work, Lyu et al. [27] a neurostimulator implant is presented. The stimulator receives power from a transmitter coil at the resonant frequency of 198 MHz. This device salvages input energy and stores it in a storage capacitor, and when the voltage reaches a threshold, releases the energy as an output stimulus. In another work, Yang et al.[28] proposed an implantable integrated circuit using closed-loop WPT to achieve deep brain stimulation. This method has proven to be effective therapeutic for Parkinson disease treatment, substantially suppressing and alleviating tremors. Figure 2.2 shows both stimulator implants.

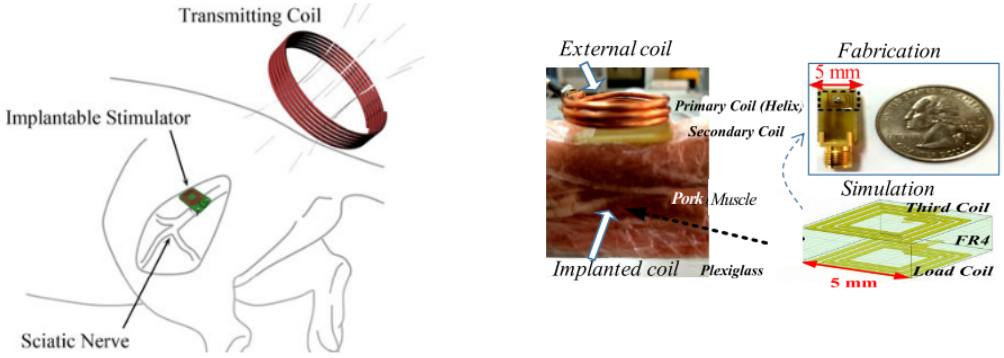

(a) Concept of neurostimulator implant on a rat [27].

(b) Experimental setup of the deep brain stimulation [28].

Figure 2.2: A few wirelessly powered implants.

[1]Cochlea - Hollow, spiral-shaped bone found in the inner ear that plays a key role in the sense of hearing. Cochlear implants are a medical prosthesis used to treat deafness.

Near-field power transfer can be classified into four groups accordingly, *(i) magnetic resonant coupling*, *(ii) inductive coupling*, *(iii) capacitive coupling* and *(iv) magneto dynamic coupling*. Near-field MRC systems seem to be the most suitable for WPT and data transmission since it takes advantage of the strong coupling that occurs between the resonant coils and usually operates at the self resonant frequency, they also can efficiently deliver power and information without causing harmful effects to the human body[29]. This type of coupling is based on Faraday's law. In 1831 Michael Faraday discovered that power could be transferred wirelessly based on the principle of magnetic induction[30]. Near-field magnetic systems, also have drawbacks as the coils greatly exceed in size, increasing the overall implant size. There are some disadvantages, such as sensitivity and alignment issues.

Although near filed WPT has shown very promising solution for biomonitoring applications, including implantable systems, one limiting factor is the low distance between the transmitting and receiving coils, which limits the usability of this systems. This is the main motivation for the investigation of Far-field energy harvesting systems, that despite the lower amount of energy harvesting compared to the near field, allow a higher distance between the transmitter and the antenna.

2.1.2 Far-Field wireless power transfer

Far-field power transfer dates back to the late 1800s, the earliest experiments were conducted by Nikola Tesla, in Colorado Springs, while attempting to transmit power wirelessly. But it was not until 1895 that the first successful RF communication was achieved by Guglielmo Marconi, which transmitted a radiotelegraphic signal beyond a physical obstacle, at a distance of about 2 kilometers[31].

In recent work, O. Gall et al. [32] demonstrated an implantable batteryless energy harvesting and telemetry storage system using 180 nm CMOS technology. This device operates at 2.4 GHz under the industrial, scientific, and medical (ISM) band. The authors also claim the device has the highest operating storage density of 450 $\mu J/mm^2$ reported to date. In Bakogianni and Koulouridis(2019).[33] a Planar Inverted-F Antenna (PIFA) was developed and tested *In-Vitro* as a dual-band arm-implantable rectenna, which works in the medical device radio communications service (401-406 MHz) and industrial, scientific and medical (902.8-928 MHz) bands.

In order to enhance the far-field power scheme a matching layer is used to boost the implantable antenna gain, this layer is made of a commercially available gel, and attached to the skin surface right above the implant, boosting the power by a factor of 2.1 times and the Power transmission efficiency (PTE) by 4.4 times. The model of this experiment is illustrated in Figure 2.3.

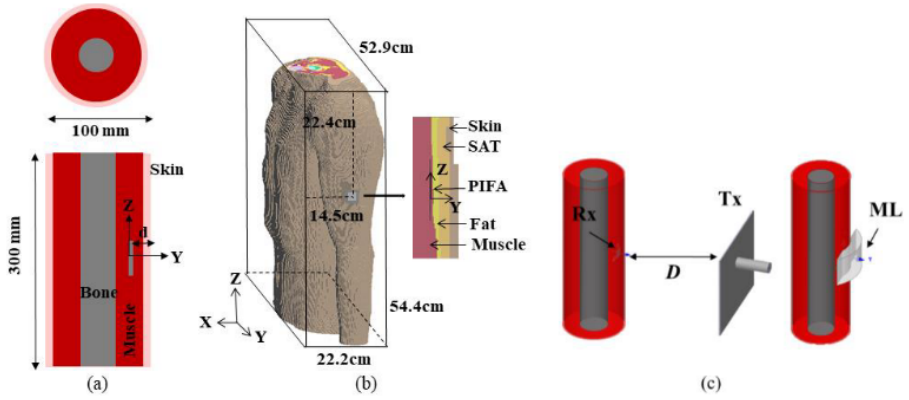

Figure 2.3: Antenna simulation environment, **(a)** Canonical human arm model **(b)** Anatomical human body (Duke model) and **(c)** Matching layer. Adapted from [33].

In applications that require wireless power transfer over a long distance, inductive or capacitive coupling mechanism cannot be utilized, as the coils will greatly exceed in size[34]. Therefore, for applications where the transmitter cannot be placed near the biomedical device, far-field systems must be used. E. Chow et al.[35] presented a miniature implantable RF powered device to measure intraocular pressure. The device uses a capacitor based power storage array to maintain continuous operation, exploiting this configuration together with an ultra low-power circuit, they demonstrated more than 24 hours operation, on an *In-vivo* ocular implant attached to a rabbit while externally powering the circuit with a 3 GHz antenna(Figure 2.4a). To power the implant the authors used a pulsating technique, optimizing the width and frequency of the pulse, along with the instantaneous RF power to rapidly charge the capacitor-based power storage array. This implantable intraocular pressure sensor can help in evaluation of patients at risk of glaucoma.

In 2015, K.Okabe et al. [36] proposed a flexible RF WPT device(Figure2.4b), intended to be implanted on the brain surface. The device acts as a neural interface for recording neural waves, and is composed by an antenna, transformer, and rectifier. It generates more than 1.5 Volts and achieves a PTE of 0.086% for an input

power of 14.5 dBm, transmitted at 10 cm distance.

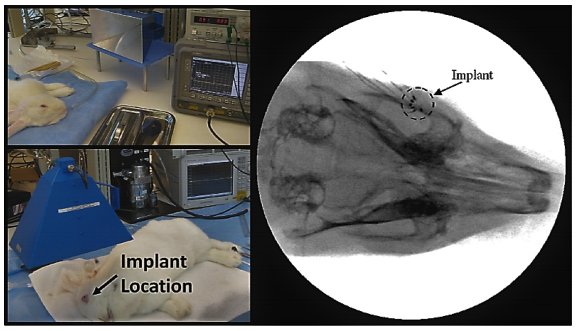

(a) RF powered intraocular pressure sensor[35].

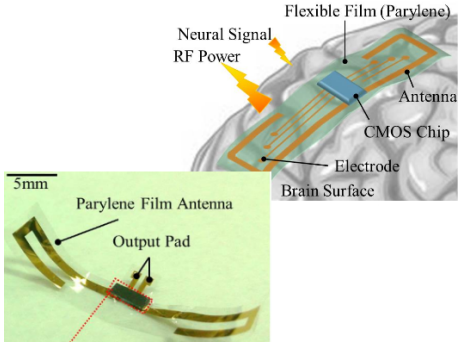

(b) RF powered implantable neural interface[36].

Figure 2.4: Examples of implantable biomedical devices powered by RF antennas.

In the far-field sector there is an emerging increase in devices using Ultra High Frequency (UHF) RFID the operating frequency band covers the range from 300 MHz to 3GHz, which covers the Scientific and Medical(902.8-928 MHz) band. Most UHF RFID systems comply with UHF Gen2 standard protocol, that operates in the 860 to 960 MHz band. Energy transfer in these systems is achieved through electromagnetic radiation, and allows a significantly higher bandwidth, consequently allowing higher data transfer rates. RFID dates back to the 1940's where it's first known use was to identify enemy and friendly aircraft's in World War II using radar technology discovered by Scottish physicist Sir Robert Alexander Watson-Watt in 1935. Watson-Watt and the British government, developed in secret the identify friend or foe (IFF) system. They placed a transmitter on each of the British planes, and when it received signals from radar stations on the ground, it began broadcasting a signal back that identified the aircraft as friendly. RFID works on the same basic concept, a signal is sent to a transponder, which wakes up and either reflects back a signal (passive system) or broadcasts a signal(active system).

Passive RFID systems have several applications in current days. They are used for asset tracking, inventory control, anti-counterfeiting and identification. The ability to read multiple tags at once with time stamps, has been an attractive feature for race timing systems. These timing systems are used in cycling, BMX, skiing and marathons. In marathon races, each athlete is assigned a specific RFID tag, used to identify the participant, and also to obtain the time it takes to reach a checkpoint

or the finish line. Some industrial warehouses also use this technology to keep track of inventory, for instance counting the number of articles that are in a cabinet, by passing a scanner that can count each product with the specific software. Both practical application cases are depicted in Figure 2.5.

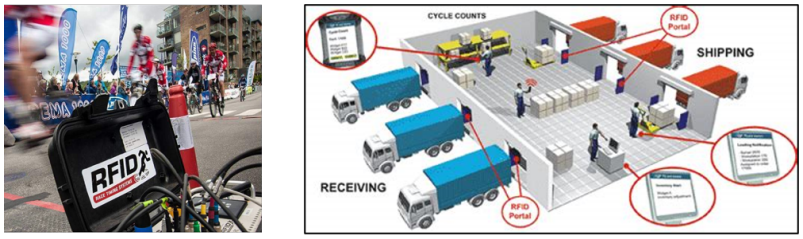

(a) (b)

Figure 2.5: Examples of some RFID applications: **a)** Cycling, race timing system. **b)** Asset tracking in industrial warehouse.

UHF RFID is also a viable solution for harvesting power as demonstrated in [37], where an epidermal bateryless electronic system with ultra thin antennas, rectifiers and voltage doublers which operates between 1 GHz and 700 MHz. This epidermal electronic device can be seen in Figure 2.6. The authors used an external RF 11 dBi antenna transmitting at 15 W, to provide sufficient RF power to light the integrated LED at a distance of 1.5 meters.

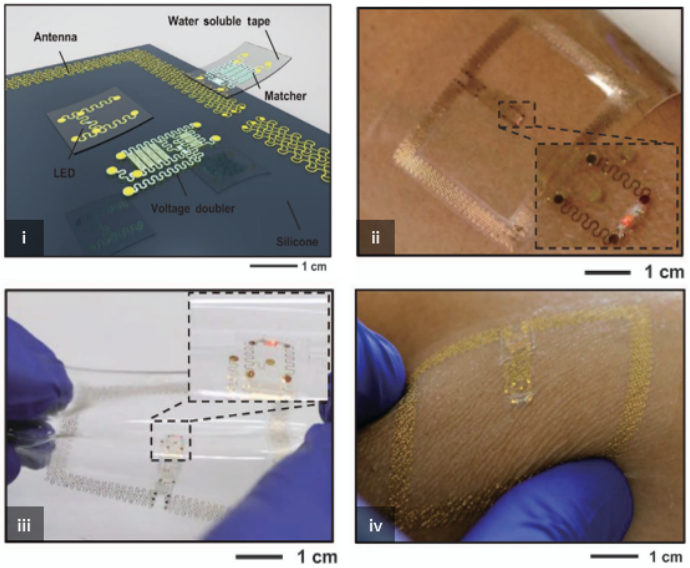

Figure 2.6: Pictures of the epidermal RF system. **i**: Device assembly diagram that illustrates modularization. **ii**: Epidermal RF system powering a red LED while on the skin **iii**: and while being stretched and **iv**: twisted on skin. Adapted from [37].

In the healthcare area, S. Niu et al.[38] showed a Wireless Body Area Networks (WBAN) that intend to be attached to the human body through on-skin sensors and rigid in-clothes circuits, for personalized health monitoring. A node from this sensor network is formed by, soft and stretchable electronics that communicates through RFID with a flexible PCB that is attached to textile above the sensor. This design removes all direct contact between rigid components and the human body. The skin-mounted sensor tags are fabricated by printing intrinsically stretchable materials onto elastic substrates to form functional strain sensors and antennas. The body area sensor network consists of multiple sensing nodes, distributed throughout the body. The nodes are detect breath, pulse and joint movement, as illustrated in Figure 2.7. The signals recorded from the nodes are sent to a smartphone via BT, and then to the cloud for storage or further analysis.

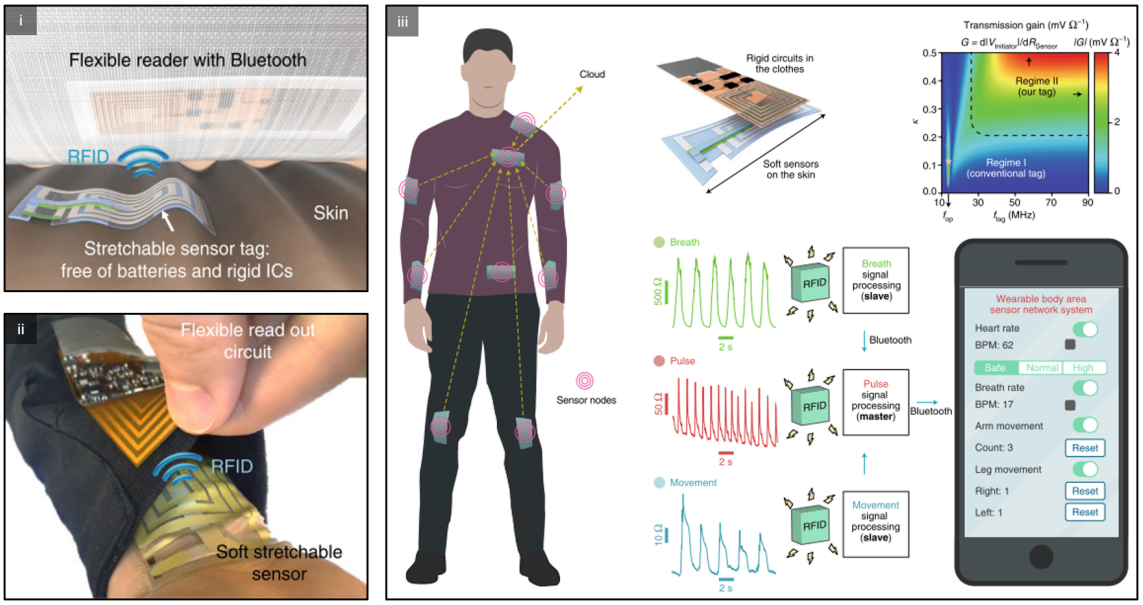

Figure 2.7: A body area network based on soft sensor nodes. **i**: Schematic of the sensor node. A stretchable sensor is conformably attached on skin. The information is wirelessly read out by a flexible printed circuit board on clothing. **ii**: Photograph of a sensor node for sensing the pulse on a human wrist. **iii**: Concept of the sensor network. Adapted from [38] and [39].

2.2 Printed and Stretched Electronics

Over the last decade, several research groups have been interested in stretchable electronics. Liquid metals are the softest and most deformable class of electrical conductors. They are inherently stretchable, and can be embedded in a elastomer without altering the mechanical properties of the composite[34]. These composites can maintain metallic electrical conductivity at extreme strains and can conformally adhere to surfaces. Liquid metals are used as, conductor wires, conformal electrodes, stretchable antennas and soft circuit boards. Liquid metals are integrated as functional components in circuits, such as sensors, capacitors and even memory devices.

Gallium based liquid metals are reliable candidates for flexible and stretchable electronic devices and RF communication platforms. Liquid Metal (LM) patterning in thin films allows for the construction of many types of antennas. The most popular approach is to fabricate LM antennas on soft and flexible substrates to realize elastic antenna designs.

In 2012 G. J. Hayes et al. [40] presents a flexible microstrip patch with multi-layer construction, that incorporates microchannels filled with LM encased in 4mm thick PDMS elastromer(Figure 2.8). This complex geometry antenna has an area of $4 \times 4cm^2$, and achieves a reflection coefficient of -6.56 dB at 3.45 GHz.

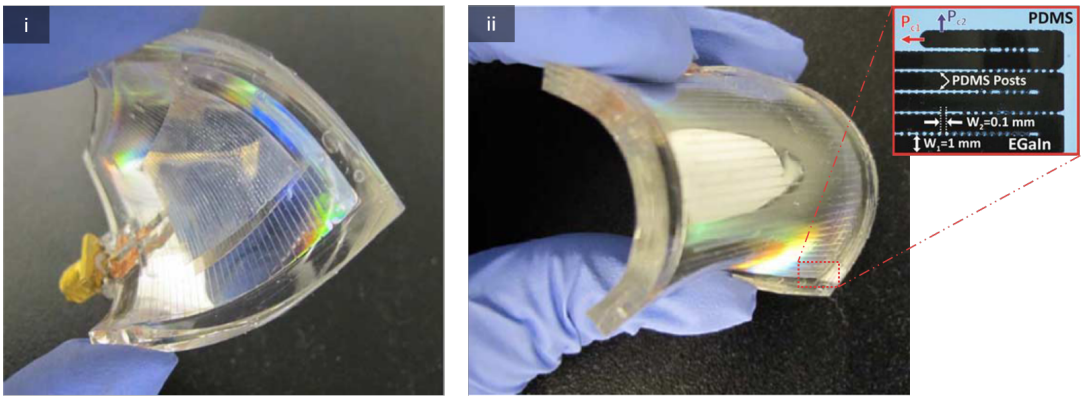

Figure 2.8: G. J. Hayes et al.[40] Multi-layer, flexible microstrip patch antenna composed of Liquid Metal (LM) encased PDMS in elastomer. **i**: Front view. **ii**: Back view.

Recent developments of flexible and stretchable skin-mounted electronics using antennas can be seen in [41]. It shows the advancements on soft, biointegrated technology using ultrathin, ultralow modulus devices that can undergo large mechanical deformations. Miniaturized, stretchable antennas represent an essential link between wireless monitoring devices that monitor various biological processes and external systems, used for power delivery, data processing and communication. The processes for wirelessly transmitting and receiving data/power to and from external devices most typically rely on integrated antennas in soft elastomers[41]. The electromagnetic performance depends on the geometry, orientation, constituent materials, and the surrounding environment. The design goal centers on maximizing the stretchability and minimizing the sizes, while maintaining electromagnetic performance.

In 2008 Kim et al. [42] introduced layouts for high frequency NFC antennas that incorporate stretchable serpentine structures for epidermal electronic devices to harvest power and transmit data when mounted on the skin. The antenna can operate effectively during extreme deformations with minimal shifts in operating frequency (0.3 MHz) for 30% strain. In 2019, Chung et al. [11] used this technique to implement a battery-free, ultrathin epidermal electronic system for vital signs monitoring in the neonatal intensive care unit(Figure 2.9). This system is comprised of two skin-like electronic devices, one for acquisition of ECG data, placed on the chest, and the other one mounts on the base of the foot to record photoplethysmograms (PPGs). Each of the devices is configured to allow simultaneous wireless data transmission and wireless power delivery through a single link. From this data, the authors are able to extract HR, heart rate variability (HRV), RR, SpO_2, and BP.

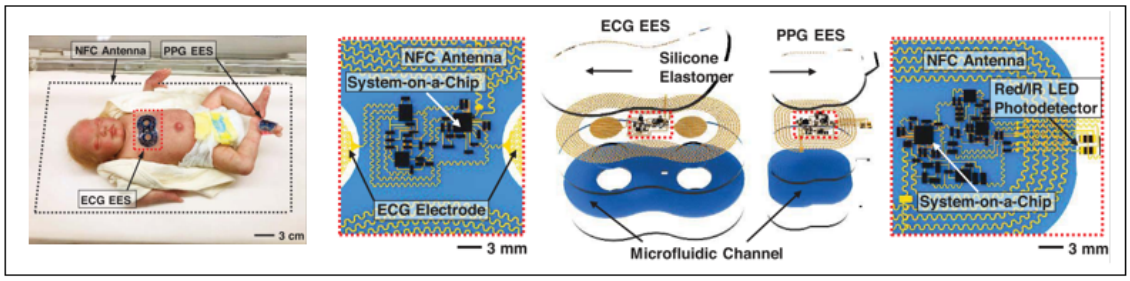

Figure 2.9: Picture and schematic of a epidermal electronic, wireless battery-free system, for vital signs monitoring in neonatal intensive care. Adapted from [11].

In recent work, Y. Fan et al. [43] proposed a miniaturized single-fed circularly-polarized (CP) microstrip patch antenna for implantable wireless communications, operating in the Industrial, Scientific, Medical (ISM) band at 2.40–2.48 GHz. The proposed antenna can be seen in Figure 2.10 and it's dimensions are 9.2 mm x 9.2 mm x 1.27 mm. This miniaturization is achieved by employing a reactive loading technique in the patch design. The slots in the patch act as a capacitor and forms a slow wave effect. By exploiting this effect the authors achieve a 21% size reduction from a conventional square shaped patch antenna.

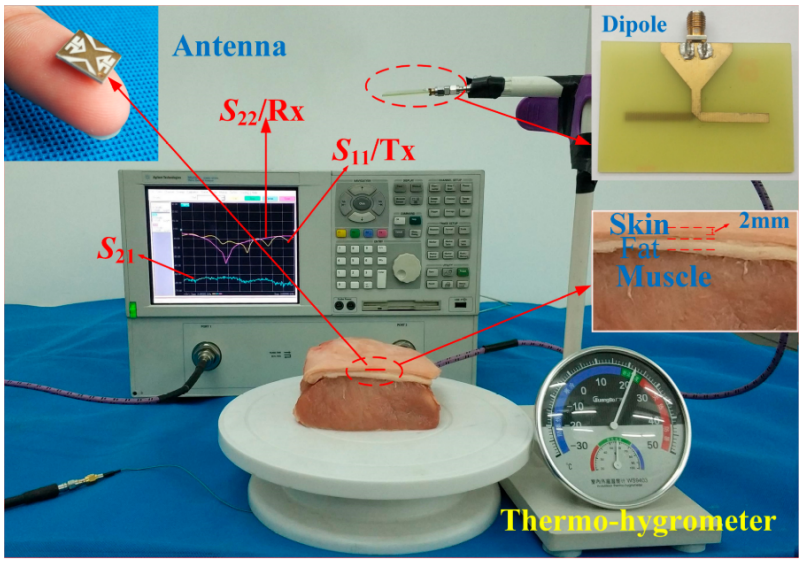

Figure 2.10: Y. Fan et al. Antenna prototype and measurement setup. From [43].

Another research focus in the last years, has been 3D antennas. The controlled assembly of complex 3D micro/nanostructures provides access to advanced classes of stretchable antennas, the highly customizable 3D shapes create a set of opportunities in properties, size, and tunability. Size has particular importance in wearable biointegrated systems[41]. Electrically Small Antennas (ESA) like the one in Figure 2.11 iv and viii, have large bandwidths and increased data transmission rates, the ESAs, find use in a wide variety of communications platforms, but their construction requires advances in printing as well as a robust antenna design so that their operating frequency, size, and impedance could be easily varied.

Figure 2.11 i and ii, show 3D helical structures antennas that are bonded to an elastomeric substrate to provide highly stretchable mechanics [41], both antennas are

NFC based for WPT. A pure textile patch antenna is seen in 2.11 iii , designed for BT wearable applications at 2.4 Ghz. This antenna maintains an output power of 12 mW at 15 cm. Figure 2.11 v, depicts the potential wearable locations of the antenna and compares the frequency stability between a serpentine and straight antenna under a dynamic applied strain. Carbon nanomaterials are also attractive choices. A thermal treatment approach enhances the mechanical properties of flexible graphite film (FGF). Figure 2.11 vi, show flexible graphite film antennas that can undergo cyclic bending without significant degradation. A vertically aligned carbon nano tube based antenna seen in Figure 2.11 vii, can undergo 13% stretching and bending to an angle of 130 while maintaining a good performance[41].

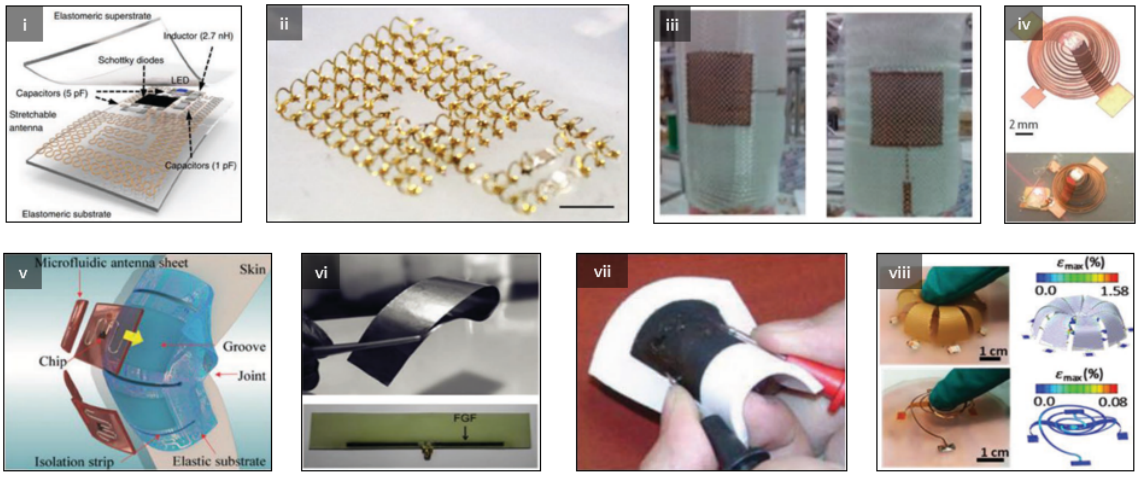

Figure 2.11: Stretchable antenna designs types from different materials. **i**: A stretchable patch antenna; **ii**: A 3D stretchable antenna with helical mesostructures; **iii**: Woven-fabric patch; **iv**: 3D NFC spiral antenna; **v**: Half-wave dipole serpentine antenna with Liquid Metal (LM); **vi**: Graphene film diapole antenna; **vii**: Vertically aligned carbon nanotubes patch antenna; **viii**: 3D Meanderline-Based Hemispherical ESA (MHESA)and HHESA. Adapted from [41].

2.3 Work Focus

This dissertation focuses on the development of a far field energy harvesting system to continuously power biomonitoring stickers. Despite the developments in the area of stretchable electronics and epidermal electronic patches by ISR-UC[44, 45, 1], these systems still rely on rigid portable batteries such as coin cell batteries and lithium-ion polymer batteries (LiPo), which limits the application of these devices. In most cases the batteries are the largest rigid component of the sticker patches, which are intended to be ultra-thin, skin-conformable and stretchable to maximize mechanical compatibility with biological tissues.

The long-term goal is to reach a point where electrophysiological data from the human body can be acquired and wirelessly transmitted, using fully passive, untethered, and batteryless patches, that interface the human skin.

Chapter 3

Far-Field Energy Harvesting

In this chapter, after a short introduction to RFID energy harvesting, a detailed description of the systems and equipment used in this work will be presented. Also initial characterization tests with rigid PCB antennas are performed and presented, which served as an initial reference point for comparison with printed and stretchable RFID antennas.

3.1 Radio frequency harvesting: Operation method

A far-field WPT system is composed of two main components: 1. The transmitting unit, which creates a radio frequency alternating current to excite an antenna, in which the antenna then emits electromagnetic waves at a given frequency. 2. The receiving/harvester part, which receives this transmitted signal though the rectenna, where it uses a reactive matching circuit, a combined voltage multiplier, and a rectifier that converts this energy to Direct Current (DC). As shown in Figure 3.1, the RF input signal is rectified during the positive cycle. The stored energy on the input capacitor C_1 during the negative cycle is transmitted to the output capacitor C_2 during the next positive cycle of the RF input signal. Thus, the voltage on C_2 is roughly two times the peak voltage of the RF source minus two times the turn on voltage of the diode.

To understand the RF energy harvesting principle one can start with one of the most fundamental equations in antenna theory, the Friis' transmission equation 3.1 which shows the relation between the terminal voltage and current of a receiving

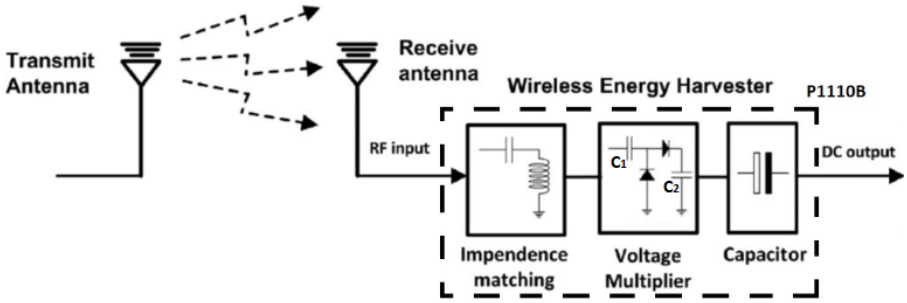

Figure 3.1: RF Harvesting system diagram.

antenna with the radiated power from a transmitting one. When a signal generator is applied to an antenna it forces a time-varying current through it's structure which produces electromagnetic radiation, therefor the radiation mechanism of any antenna is based on the acceleration of electric charge.

$$P_{av} = \left(\frac{\lambda}{4\pi d}\right)^2 \times D_{RX} \times P_{EIRP} \tag{3.1}$$

The above equation relates the free space path loss[1] $(\lambda/4\pi d)^2$, antenna gains and wavelength with the power received and the power transmitted, and gives a fundamental limit to the available power as a function of distance. Where d represents the distance between the Rx and Tx antennas, λ is the free space wavelength for the given frequency, D is the directivity that describes the antenna radiation intensity in a given direction and $P_{EIRP} = P_{Tx}D_{Tx}$ is defined as the equivalent isotropic radiated power (EIRP). The available power P_{av} is defined as the maximum power that can be extracted from an antenna and can be delivered to the load (i.e., power at the input of the RF energy harvester)[46].

Solving equation 3.1, we can see that more power is lost at higher frequencies or that path loss is higher for higher frequencies. The resulting path loss at a distance of 1 meter, for the frequency of 915 MHz is 31.68 dB and for 2.4 GHz is 40.05 dB.

[1]Free space path loss is the loss in signal strength of an electromagnetic wave that would result from a line-of-sight path through free space, with no obstacles nearby to cause reflection or diffraction.

3.2 System Characterization

The far-field WPT system used in this dissertation will be discussed ahead.

3.2.1 Transmitter module

The transmitter side of the system is composed by an RF signal generator and an antenna. For the RF signal generator we used a RFID reader unit, that is intended for RFID tag reading. The reader used was a SparkFun board, with the ThingMagic M6e-Nano UHF RFID reader that can be seen in Figure 3.2. This board has a PCB antenna and an Hirose U.FL connector to connect an external antenna. Also the UHF RFID module allow us to write proper firmware to control the Tx power and frequency(859-930 MHz) and as well enabling the ability to write and read data stored in RFID tags by using ThingMagic Mercury Application Programming Interface (API) software or the ThingMagic Universal Reader Assistant. Its characteristics are shown in table 3.1.

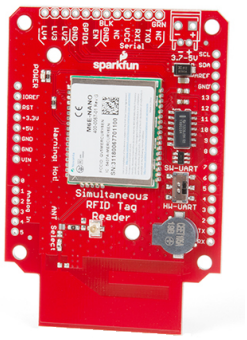

Figure 3.2: Picture of the SparkFun M6e-Nano UHF RFID Reader.

RFID protocol support	IS0 18000-63
Output frequency range	859MHz to 930MHz
RF power output	0 dBm to +27 dBm (500 mW)
Communication interface	TTL Logic Level UART serial port
Maximum tags read rate	Up to 200 tags per second
Maximum tag read distance	Over 4.5 meters (using an appropriate antenna)

Table 3.1: JADAK Thingmagic M6e-Nano UHF RFID reader specifications.

As mentioned before, the SparkFun board has a connector to attach an external antenna and this grants us the capability of choosing one external antenna with the required specifications for the developed application, such as antenna gain, frequency and polarization. The external antenna selected can be seen Figure 3.3 it's characteristics are presented in Table 3.2. The resulting combination of the reader unit and external antenna yields a Peak Effective Isotropic Radiated Power (PEIRP) of 2 Watts. $P_{EIRP} = 27dBm + 6dBm = 33dBm$

Figure 3.3: Picture of the UHF RFID antenna.

Gain	6 dBi
Frequency range	860MHz to 960MHz
Maximum power output	100W
Impedance	50 Ω
Polarization	Linear vertical

Table 3.2: External UHF RFID antenna specifications.

In addition to this RFID and antenna module, another Tx was used, the TX91503 PowerSpot from Powercast. This device is part of the commercially available Powercast lineup, and is specifically designed as a RF transmitter to wirelessly recharge compatible devices, such as headphones, smart watches and wearables. It advertises an appealing power output of 3 Watts PEIRP for its small form factor, this Tx specifications are listed in Table 3.3.

Figure 3.4: Picture of the Powercast PowerSpot TX91503.

Power modulation protocol	Direct Sequnce Spread Spectrum (DSSS)
Output frequency	915 MHz Center Frequency
RF power output	3W EIRP (34.77 dBm)
RF Beam pattern	70^{o} width, 130^{o} height Horizontal Polarization
Dimensions	18.6 x 5.3 x 3.6 cm

Table 3.3: Powercast TX91503 transmitter specifications.

3.2.2 Harvester module

For this project, we first start with a commercially available RF harvester module and rigid PCB antennas, in order to register the maximum harvesting energy with this setup, which will be later compared with the printed stretchable antennas produced in this work. The deviced used was the Powercast P1110B development board. This evaluation tool helps to assess the harvester capability's and limitations and better understand the behavior of RF waves over the distance for different environments. This development tool seen in Figure 3.5a is build around the P1110B 915Mhz module, which converts RF energy into DC power. The P1110B has a high conversion efficiency, greater than 70%. It's operation ranges from -5 dBm to 20 dBm input RF power and it can be configured to output different voltage levels to support Li-ion and Alkaline battery recharging (4.2V and 3.3V respectively).

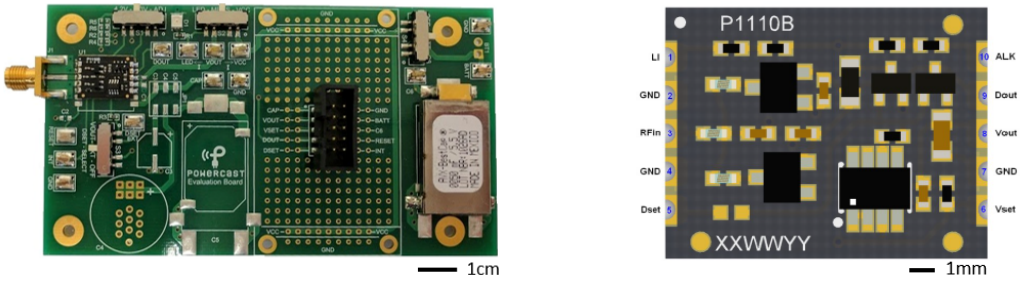

(a) Powercast evaluation board.

(b) P1110B pin configuration.

Figure 3.5: Powercast P1110B energy harvesting device.

In this development kit there were included two types of 915 MHz PCB antennas, with different gains. A vertically polarized directional(122° horizontal, 68° vertical energy pattern) patch antenna with 6.1 dBi of gain(Figure 3.6a) , and a

vertically polarized omni-directional(360° energy pattern) dipole antenna with 1.0 dBi gain(Figure 3.6b). Both antennas have a SMA connector to interface with the Powercast evaluation board.

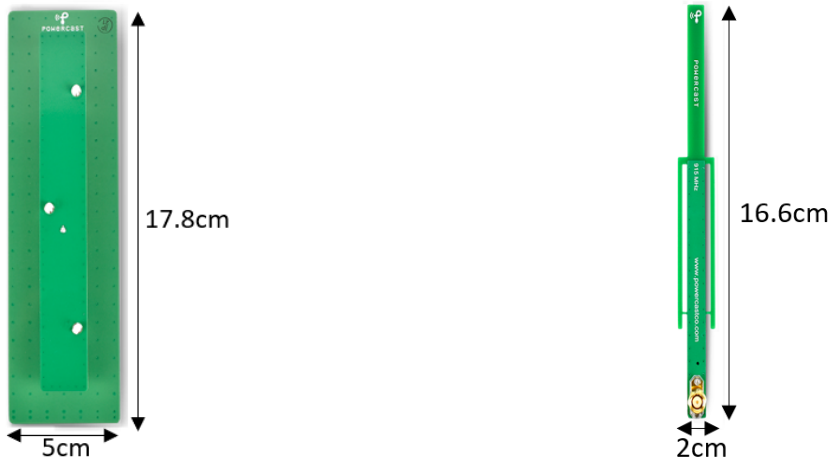

(a) Powercast 6.1 dBi antenna.

(b) Powercast 1 dBi antenna.

Figure 3.6: Assortment of Powercast antennas.

3.2.3 RF harvester classification

The purpose of this evaluation is to analyze the behavior of the harvester system for different types of loads, and classify the amount of harvested power, that the system can supply, while using the 6 dBi and the 1 dBi antennas. To obtain the amount of harvested power and to simulate a bio-monitoring application, we tested a group of four distinct loads for each antenna. The load resistors values selected for the experiment, were 68Ω, 330Ω, 2.2$k\Omega$ and 4.7$k\Omega$. The output power of the harvester can be calculated using Ohm's law: $P_{out} = V_{out} \times I_{out}$ or $P_{out} = V_{out}^2 / R_{Load}$.

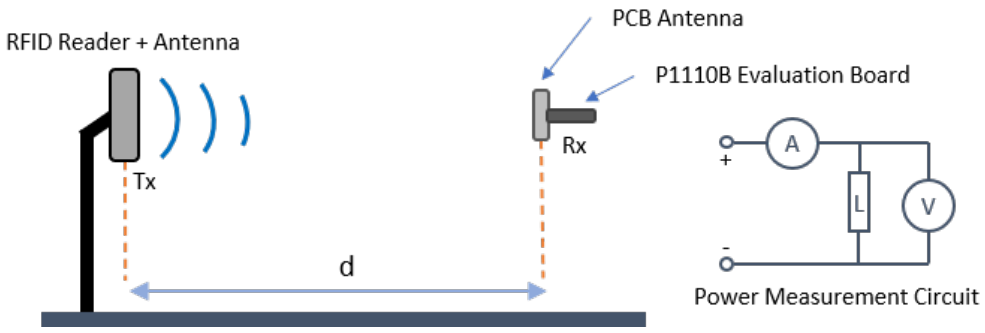

Figure 3.7: Schematic of the RF harvester classification method.

Figure 3.7 depicts the RF harvester evaluation, this method began with, setting up the RFID and antenna Tx module at 27 dBm(500mW)(Refer to appendix A), and placing the P1110B evaluation board harvester with the Rx antenna at a distance of 10 cm. Then this distance was incremented by 10 cm until the distance reached 1 meter, after that the increment increased by 50 cm until the distance between the Tx and Rx reached 3 meters. Every time the distance was increased, voltage and current measurements through the load were acquired. This process was repeated for both the 6 dBi and 1 dBi antennas, and the results of the total amount of power havested for each antenna can be seen in Figure 3.8 and Figure 3.9 respectively.

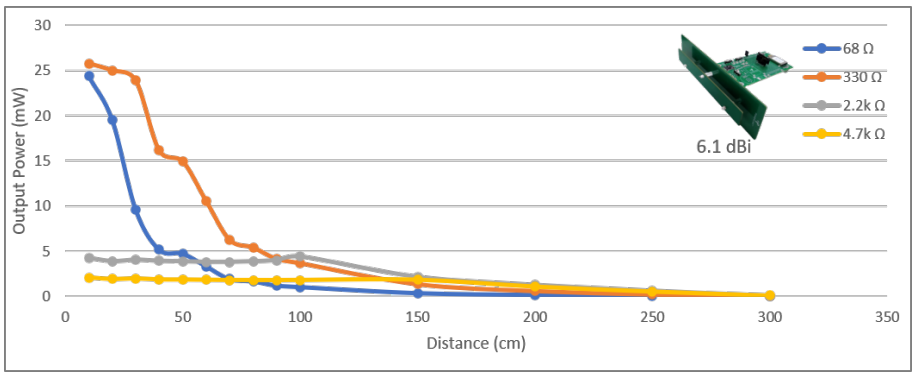

Figure 3.8: Harvested power over distance for the Powercast 6.1 dBi antenna.

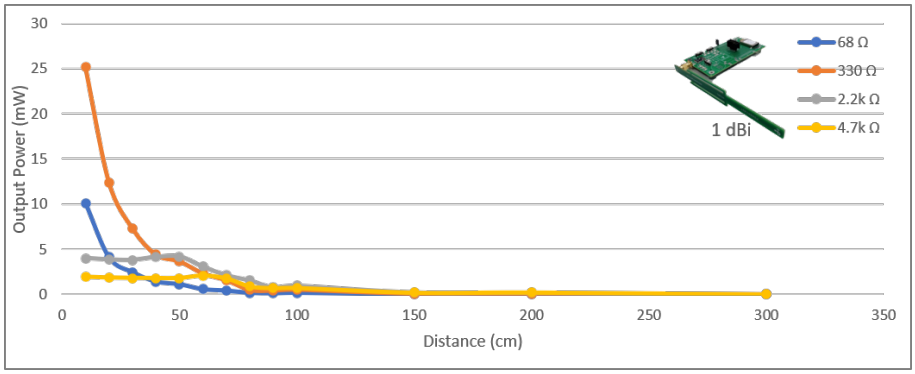

Figure 3.9: Harvested power over distance for the Powercast 1 dBi antenna.

In order to access the viability of using the Powercast P1110B RF harvester, we fabricated a custom RF harvester in a effort to miniaturize the harvester system. This manufactured harvester employs a well known design for this type of systems, the Dickson charge pump circuit using schottky diodes, which is represented in Figure 3.10. The output of the Dickson circuit was then connected to step up DC

\DC converter(LTC3105 by Linear Technology) to produce enough voltage to power a Microcontroller Unit (MCU).

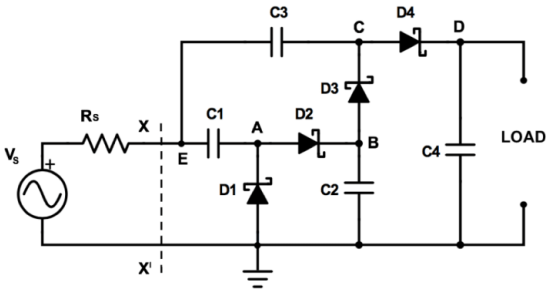

Figure 3.10: Schematic of the 2-Stage Dickson charge pump. From [47].

The fabricated RF harvester, was first designed using Eagle Autodesk PCB design software, then the layout was transferred to the FR-4 PCB, and then chemically etched(Refer to appendix B). The electrical components (diodes, capacitors, etc) where surface mounted using solder paste and a heat gun. A picture of the fabricated device is shown in Figure 3.11. To classify the fabricated harvester and compare it with the P1110B, both harvester were subject to the same test, under the same conditions. The used method was similar to the previous classification, this time, only the 330Ω load resistor was used. For the same distance of 40 cm, the P1110B harvested 4.375 mW, and the fabricated harvester was only able to harvest 1.75 mW. From this testing we concluded that we're unable to miniaturize the device without sacrificing efficiency. Another motivation behind the effort to build this custom RF harvester was the possibility to fabricate the circuit on a flexible substrate, therefore reducing the rigid components and increasing the mechanical compatibility with biological tissues, such as the skin.

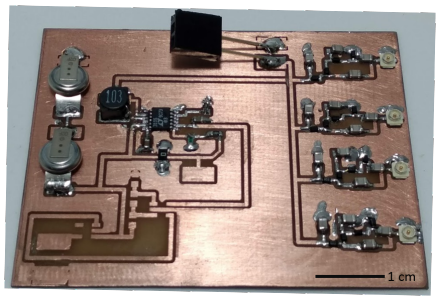

Figure 3.11: Fabricated RF to DC harvester.

3.2.4 Chapter Summary

In this chapter, we evaluated the rigid PCB antennas, and characterized the P1110B harvesting system. From the obtained results we built Table 3.4 , that represents how much power the P1110B evaluation board harvested for both PCB antennas for the 330 Ω load. We can observe that, the maximum power output the harvester can provide is 26 mW, and the harvested power drastically decreases with the increase in distance. At 1 meter the power harvested for the 6.1 dBi patch antenna was 3.7 mW, and for the 1 dBi omnidirectional antenna was just 0.38 mW, in line of sight configuration. We also evaluated our fabricated RF harvester, that outputted 1.75 mW of power to the 330Ω load at a distance of 40 cm, while using the 1.0 dBi omnidirectional antenna. Taking this result into account, we decided to rely on the commercial P1110B for the time being, but acknowledge that harvester optimization should be revised in future work.

Distance (cm)	6.1 dBi Patch antenna	1.0 dBi Omnidirectional antenna
10 cm	25.77 mW	25.13 mW
20 cm	25 mW	12.38 mW
30 cm	26.89 mW	7.285 mW
40 cm	16.14 mW	4.39 mW
50 cm	14.95 mW	3.64 mW
60 cm	10.57 mW	2.32 mW
70 cm	6.27 mW	1.56 mW
80 cm	5.42 mW	0.49 mW
90 cm	4.15 mW	0.42 mW
100 cm	3.68 mW	0.38 mW

Table 3.4: Output power of the P1110B harvester for the 330 Ω load resistor, for the different PCB antennas. Measurements on free space medium.

Chapter 4

Antenna Design and Optimization

The goal of this chapter is to design, optimize and implement printed stretchable antennas, to substitute the rigid PCB antennas. To do so, we first start by replicating the design in the rigid PCB, classify, measure and compare them. Then, we optimize the antenna design, taking into the account the theory, the previous works on printed antenna design and characterization, simulation software, and experimental measurements. Materials and methods will be reviewed along with the results and its discussion.

4.1 Antenna fabrication using flexible materials

Standard antennas are generally developed using highly conductive metals such as copper, which results in highly efficient antennas, but lacks mechanical flexibility. Such limitation narrows the application range of copper-based antennas to rigid surfaces. Flexible antennas, on the other hand, adopt the mechanical properties of the surrounding substrate. The attractive mechanical, electromagnetic, and chemical properties of gallium-based liquid metals make them safe-to-handle, reliable candidates for flexible and stretchable electronic devices and radio-frequency communication platforms[41]. The semi-liquid conductor allows soft antennas to withstand mechanical deformation, such as stretching, twisting, folding and bending, when combined with flexible substrates, and are able to return to their original shape after deformation.

As a starting point towards a reliable flexible antenna intended for epidermal applications, we started by replicating the antenna design of the Powercast 1 dBi omnidirectional antenna. This design was chosen due to its reduced size and low profile in comparison with the 6.1 dBi one. The fabrication process of this antenna began by choosing a suitable flexible substrate to replace the FR-4 substrate, which is the material used in the PCB version of this antenna.

Figure 4.1: Powercast 1 dBi omnidirectional antenna. **i**: Rigid version. **ii**: Fabricated flexible version. **iii**: Fabricated flexible version on human subject forearm.

The substrate selected for the antennas was Elastica liquid PVS Latex (FORMX^{TM}), and the conductive ink was made with silver nanoparticles and EGaIn. The ink composition can't be disclosed in this dissertation, it was used due to the fact that it is flexible, highly conductive($9.7 \times 10^4 S/m$) and can easily be printed over latex. The flexible 1 dBi antenna is shown in Figure 4.1 ii, and the fabrication process is represented in Figure 4.2, where the step by step process is described.

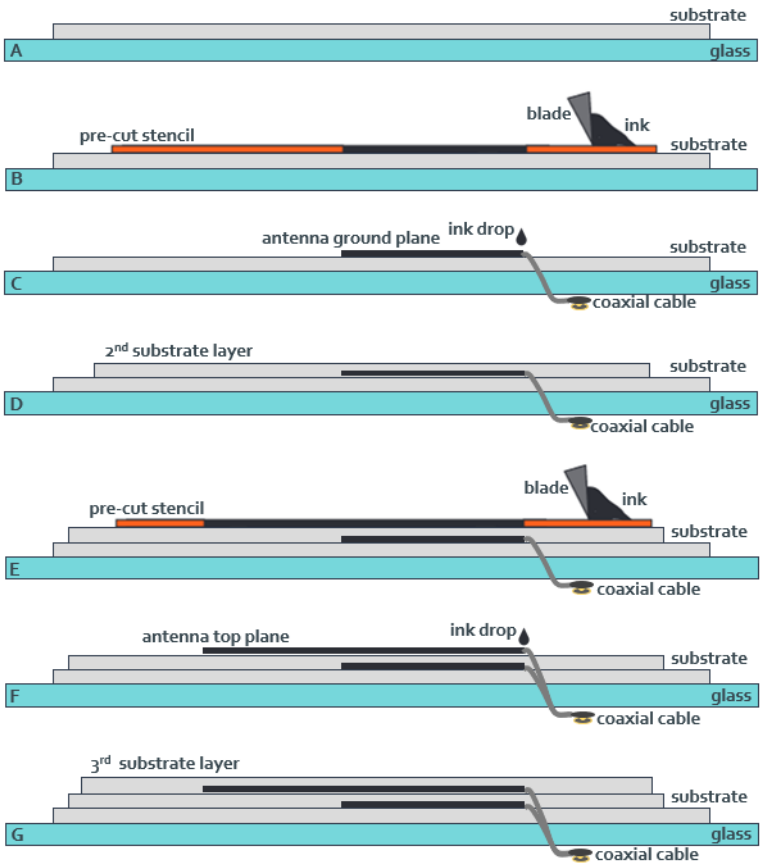

Figure 4.2: Schematic of the 1 dBi antenna fabrication process. **A**: The latex substrate is cured on top of a glass in order to cure uniformly. **B**: A previously cut stencil is placed on the substrate and the ink is spread using a sharp blade or spatula, **C**: to form the antenna ground plane. A coaxial cable terminal is connected to the ground plane with a drop of ink. **D**: Another latex layer is cured on top of the antenna ground plane. **E**: A previously cut stencil is placed on top of the second layer and the ink is spread using a sharp blade or spatula, **F**: to form the antenna top plane. The other coaxial cable terminal is connected to the top plane of the antenna with a drop of ink. **G**: A third layer of latex is cured to encapsulate the antenna.

4.1.1 Antenna evaluation

To evaluate the characteristic of the antennas a Vector Network Analyzer (VNA) was used to measure the Scattering parameters also known as S-parameters, which quantify how RF energy propagates through multi-port networks. This work will mostly reference the S_{11} which is the most commonly quoted parameter in regards

to antennas. The S_{11} is defined as the ratio of the reflected power over the input power at a particular frequency, which represents how much power is reflected from the antenna and hence is known as the reflection coefficient[48]. Figure 4.3 shows the visual diagram of how S-parameters are linked for a two port network, where for this application Device Under Test (DUT) is an antenna.

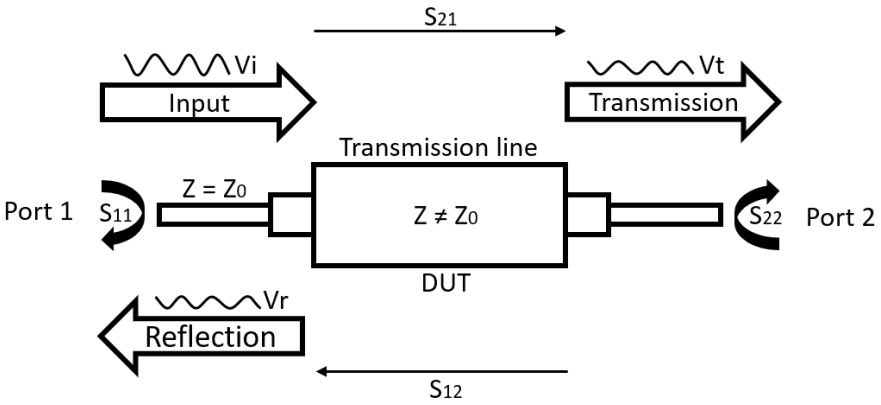

Figure 4.3: Visual interpretation of the S-parameters for a two port network.

Another important parameter derived from S_{11} is the Voltage Standing Wave Ratio (VSWR) obtained from equation 4.1 where Γ is the reflection coefficient. The VSWR is always a real and positive number for antennas. The smaller the VSWR, the better the antenna is matched to the transmission line and more power is delivered to the antenna. The minimum VSWR is 1.0, which indicates that no power is reflected from the antenna, which is ideal to achieve maximum power transfer.

$$VSWR = \frac{1 + |\Gamma|}{1 - |\Gamma|} \tag{4.1}$$

It is important to state that VSWR by itself is not sufficient to determine if an antenna is working properly, VSWR measures how much power is delivered to an antenna, but it does not mean that the antenna radiates all the power it receives[49]. The relation between the reflection coefficient and the percentage of reflected power is in part listed in Table 4.1.

Following the above discussion, we can now examine the S_{11} plots obtained with the VNA(NanoVNA-F by BH5HNU) for the rigid and flexible 1 dBi antennas. Figure 4.4 shows the S_{11} return loss of the rigid and soft antenna, versus the frequency.

VSWR	Reflection Coefficient Γ	Reflected Power %	Reflected Power dB
1.0	0.000	0.00	-∞
1.5	0.200	4.00	-14.0
2.0	0.333	11.10	-9.55
3.0	0.500	25.00	-6.00
4.0	0.600	36.00	-4.44

Table 4.1: Correlation of VSWR and reflected power. Adapted from [50]

It is seen that the center frequency of the rigid antenna is 900 MHz with -16.466 dB return loss and a VSWR of 1.354 while the flexible one center frequency is 1014 MHz with -10.999 dB return loss and 1.785 VSWR.

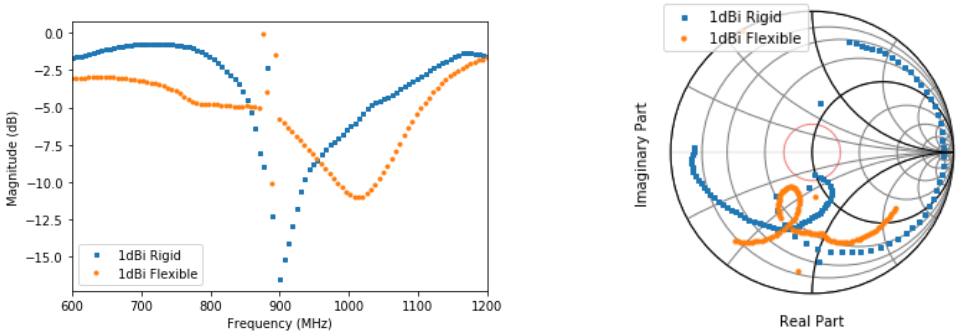

(a) S_{11} Return Loss

(b) S_{11} Smith chart

Figure 4.4: S_{11} parameters for the rigid and flexible 1 dBi antenna.

Given that the permittivity of latex ($\varepsilon_r \approx 3.31$) [51] and the FR-4 ($\varepsilon_r \approx 4.35$)[52] are different, some differentiation in the obtained harvested power measurements should be present when comparing the fabricated antenna with the rigid one. It can be concluded that the flexible antenna has 8.6 dB more attenuation than its rigid counterpart. Also it is relevant to note that there is some Global System for Mobile Communications(GSM) noise in the measurements throughout this dissertation, this happened because the data acquisition with the VNA wasn't made inside an anechoic chamber, which would have absorbed the reflections of the electromagnetic waves.

Although with the data collected from the previous analysis one can evaluate if the antenna is closely matched with the harvester in terms of impedance and frequency, the total harvested energy that the system can provide still needs to be quantified. The method devised to evaluate the amount of power the antenna and harvester

combo can supply, comprised of: on the transmitter side, configuring the RFID reader module to full power (500mW) and setting the RF frquency to 915 MHz. On the Rx side, the antenna with the P1110B harvester was placed at a fixed distance of 30 cm and a 35 mF super-capacitor was connected to the output of the harvester. With this approach we can measure the time it takes to charge the super-capacitor and calculate the total energy harvested by using equation $E = P \times t$.

We can measure the time the super-capcitor takes to charge to a certain voltage, then calculate the energy stored at such voltage and the total power harvested in that time. This is done by making use of equation $E_{cap} = \frac{C \times V^2}{2}$ and equation $E = P \times t$

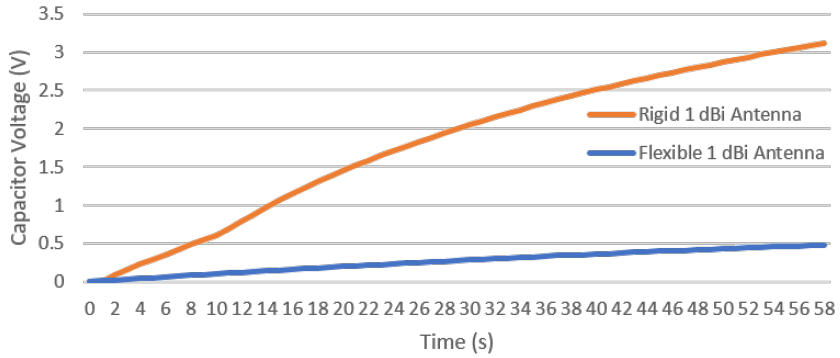

Figure 4.5: Measured capacitor voltage at the harvester output. Comparison between the rigid 1 dBi PCB antenna and the flexible 1 dBi antenna. Both antennas where placed at a distance of 30 cm from the transmitter.

Figure 4.5 shows the measured output voltage at the harvester for both the antennas at a distance of 30 cm. It can be observed that the super-capacitor charge time for the flexible antenna is very slow and amounts to a total power of 66.37 μW in a 60 second window. Thus, it can be concluded that this antenna design with the flexible material was not successful as it does not satisfy the power requirements for the bio medical application we have in mind, which should be greater than 5 mW for this distance.

4.1.2 Antenna geometry and multi-materials

Given that the results for the total harvested power with the previous antenna design was insufficient for this work objectives, other antennas designs supported by the literature were considered. The new antenna design selected was a folded dipole antenna presented in recent work by A. Thielens et al.[53, 54] where the authors had evaluated the viability of the design for WBAN.

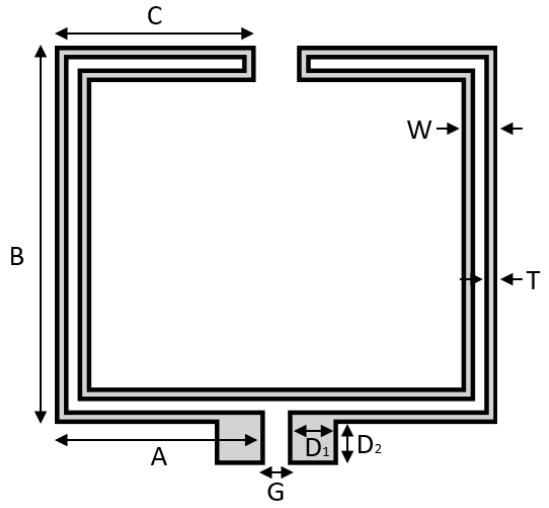

(a) Design layout.

Parameter	Dimensions (mm)
A	22.5
B	41
C	21.5
D_1	5
D_2	4.5
W	3.5
T	1
G	3

(b) Parameters table.

Figure 4.6: Folded dipole antenna layout with design parameters. Adapted from [53]

Based on their work, we began manufacturing similar antennas with the same layout, but utilizing different substrates. Figure 4.7 exhibits the assortment of the evaluated antenna series. The 2D layout was computer modeled from the parameters in Figure 4.6 and then recreated on different substrates. The dielectric properties of the substrate play an important role in achieving the desired performance of the antenna. One important property of a dielectric material is its permittivity (ε) which quantifies the ability of a material to be polarized by an electric field. Another important property of the dielectric is the dissipation factor or loss tangent ($tan\ \delta$). It measures the electrical energy absorbed and lost (power dissipation) when electrical current is applied to the material.

The first substrate used was FR-4, which is standard in PCB fabrication. The FR-4 is a composite material composed of woven fiberglass cloth with an epoxy

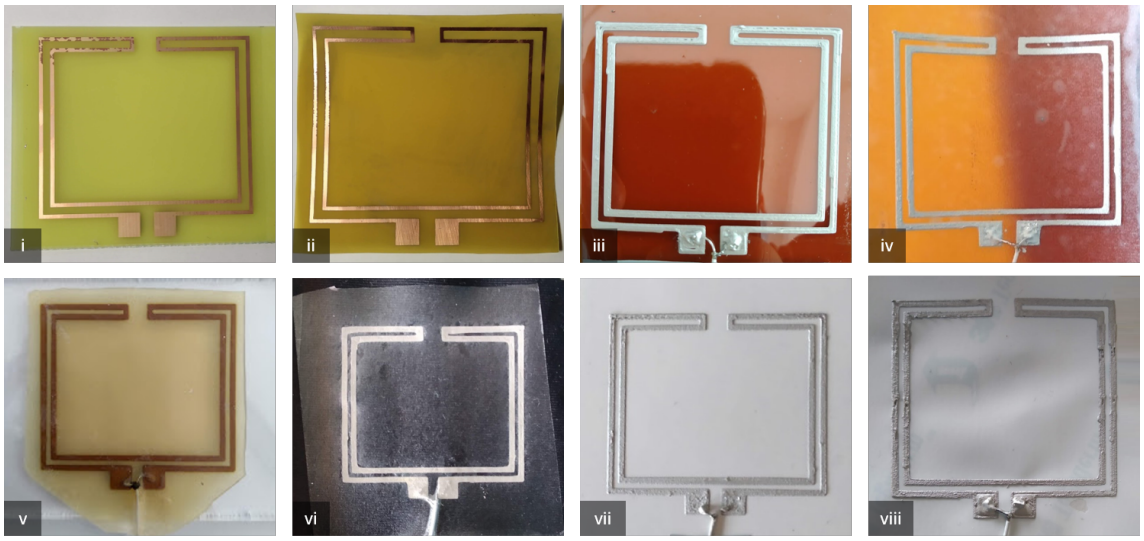

Figure 4.7: Pictures of the eight folded dipole fabricated using different materials. From left to right: **i**: Chemically etched antenna on rigid FR-4 substrate. **ii**: Chemically etched antenna on Kapton polymide flexible film. **iii**: Voltera^{TM} V-One printed antenna on flexible kapton substrate using Ag ink. **iv**: Voltera^{TM} V-One printed antenna on flexible kapton substrate using Ag ink, with Thermoplastic Polyurethane (TPU) encapsulation. **v**: Screen printed antenna on stretchable latex substrate using Ag ink, with latex encapsulation. **vi**: Voltera^{TM} V-One printed antenna on textile substrate using Ag ink, with TPU encapsulation. **vii**: Voltera^{TM} V-One printed antenna on tattoo paper(Silhouette) substrate using Ag ink. **viii**: Voltera^{TM} V-One printed antenna on Tegaderm^{TM}(3M^{TM}) substrate using Ag ink.

resin binder that is flame resistant (FR). The antenna layout was patterned over a presensitized photo resist $1.6mm$ PCB(M.G.Chemicals 600 Series - Positive Presensitized Copper Clad Boards) using laser ablation to remove the photo-resistive layer and expose the copper laminate. Then it was chemically etched using peroxydisulfuric acid($Na_2S_2O_8$) to remove the exposed cooper. Afterwards the sheet is rinsed with acetone to remove the remaining photo-resistive layer, resulting in the antenna shown in Figure 4.7i. Despite not being flexible, this material was chosen for comparison against the other flexible substrates, since it is industry standard for microstrip antennas.

The second substrate used for the antenna was a flexible Kapton polymide film with a copper layer. The film used had a thickness of $0.2mm$ and the fabrication process was similar to the FR-4 substrate, the antenna layout was also chemically

etched using the same process described above. The main difference between the two described antennas is that the Kapton polymide is flexible, due to it's thickness and polymer properties.

For the antenna in Figure 4.7iii, the antenna layout was fabricated using the silver conductive ink previously described in section 4.1 and printed on Kapton tape with Voltera V-One, PCB printer. The exact same process is used to fabricate the antenna in Figure 4.7iv, the difference being, a thin 50 micron TPU layer is added on top, to encapsulate the antenna, protecting the conductive trace and increasing its longevity. In Figure 4.7v, the antenna fabrication method is exactly the same as for the flexible Powercast 1 dBi antenna, described in section 4.1.

Another substrate used was a semi-elastic Lycra mesh, the antenna layout was patterned using the Voltera PCB printer with silver conductive ink. After the patterning, the coaxial cable is connected using the ink, and then TPU layer is heat pressed against the textile, encapsulating the antenna(Figure 4.7vi).

The same printing method was applied to antennas 4.7vii and 4.7vii, the substrate used was tattoo paper and Tegaderm^{TM} respectively.

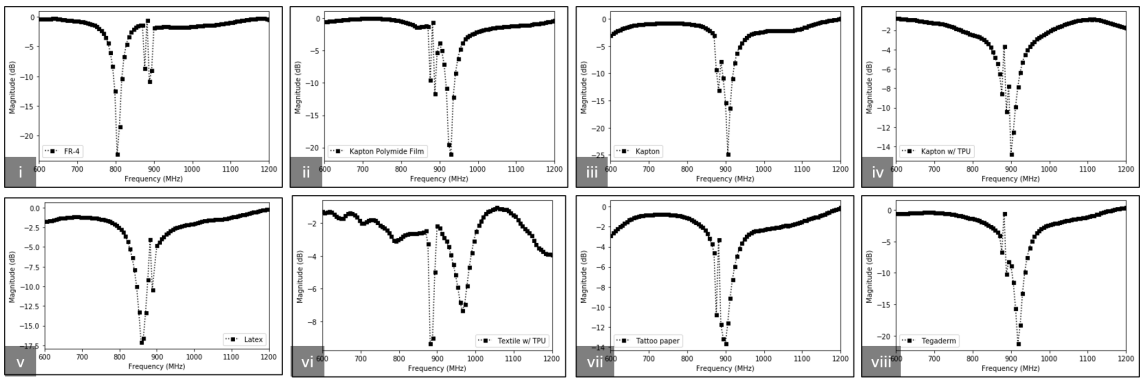

Figure 4.8: S_{11} Plots for the eight antennas presented in Figure 4.7 From left to right: **i**: Antenna on rigid FR4 substrate. **ii**: Antenna on flexible Kapton polymide film. **iii**: Antenna on flexible Kapton substrate. **iv**: Antenna on flexible Kapton substrate with TPU encapsulation. **v**: Antenna on stretchable latex substrate, with latex encapsulation. **vi**: Antenna on stretchable textile substrate with TPU encapsulation. **vii**: Antenna on stretchable tattoo paper(Silhouette) substrate. **viii**: Antenna on stretchable Tegaderm^{TM}(3M^{TM}) substrate.

Each of the antennas were evaluated using the VNA to characterize their properties, and compare the effect of using different substrates. The S_{11} plot of the selection is shown in Figure 4.8, where it's visible the center frequency change.

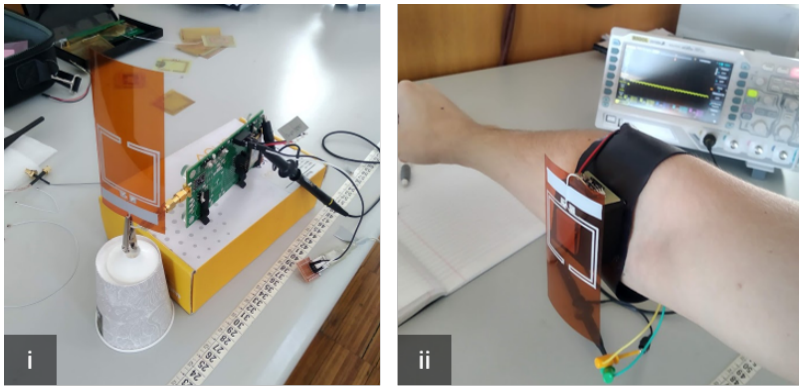

Figure 4.9: Folded dipole WPT experiment setup. Antenna subject to: **i**: Free space medium, and **ii**: human body (forearm) environments.

Then each antenna was connected to the PB1110B RF harvester, to evaluate the amount of power it could supply, to a 330 Ω load at a fixed distance of 30 cm. The experiment was conducted in two configurations, one with the antenna on free space and the other with the antenna on human body. During this experiment it was found that the direct placement on skin nullified all the antennas which amounted to zero harvestable power. To counter this effect, the antennas were offsetted 2.5 cm from the human body using a 3D printed plastic spacer, as seen in Figure 4.9ii.

The total amount of power harvested for each antenna configuration is resumed in Table 4.2, once again the harvested power results fall short of what is required to power a biomedical device, but is enough to power an LED, as seen in Figure 4.10.

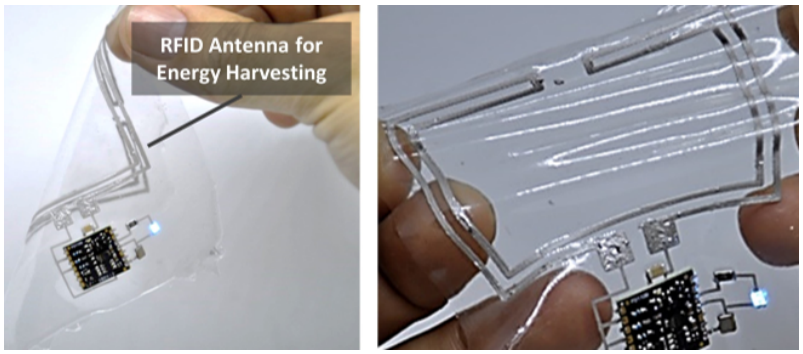

Figure 4.10: Stretchable folded dipole antenna with P1110B harvester wirelessly powering an LED.

Antenna Parameter	Antenna I	Antenna II	Antenna III	Antenna IV	Antenna V	Antenna VI	Antenna VII	Antenna VIII
Conductive Trace Material	Copper	Copper	Ag EGaIn Ink	Ag EGaIn Ink	Ag EGaIn Ink	Ag EGaIn Ink	Ag EGaIn Ink	Ag EGaIn Ink
Substrate	FR-4	Flexible Kapton Polymide Film	Kapton	Kapton	Latex	Textile	Tattoo Paper	Tegaderm
Fabrication Method	Etching	Etching	Voltera	Voltera	Screen Print	Voltera	Voltera	Voltera
Encapsulation	x	x	x	TPU	Latex	TPU	x	x
Frequency	804 MHz	930 MHz	906 MHz	900 MHz	858 MHz	966 MHz	900 MHz	918 MHz
Return Loss	-23.063 dB	-20.986 dB	-24.816 dB	-14.776 dB	-17.074 dB	-7.333 dB	-13.654 dB	-21.216 dB
VSWR	1.151	1.196	1.122	1.446	1.326	2.508	1.524	1.190
Average Power on FreeSpace	1.03 mW	4.67 mW	3.27 mW	2.37 mW	1.41 mW	0.62 mW	2.37 mW	3.27 mW
Average Power on Body (2.5 cm)	0.51 mW	2.67 mW	1.15 mW	0.83 mW	0.74 mW	0.26 mW	0.74 mW	2.92 mW

Table 4.2: Fabricated folded dipole antennas specifications and measured values.

4.2 Planar Inverted-F Antenna

The PIFA is generally classified as a monopole antenna, it is a low profile modification of the quarter wave monopole, and belongs to the category of unbalanced antennas. Figure 4.11 shows the configuration of this type of antenna. A PIFA consists of a ground plane, a dielectric, a radiating planar element, a feed pin, and a shorting pin connecting the two planes. According to the literature, the PIFA shows robustness when in close proximity with the human body[55].

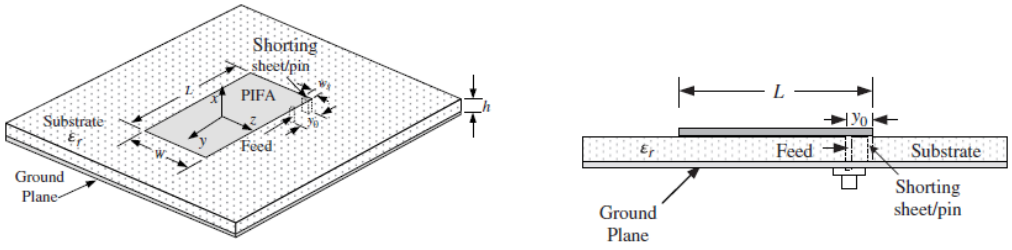

(a) 3D view. (b) Side view.

Figure 4.11: Basic PIFA design. Adapted from [48].

In respect of its performance, the current distribution of a $\lambda/4$ antenna has a peak on the center of the patch, and it goes to zero at the edges. The voltage is out of phase from the current, starting from a positive at one edge to the negative at the other edge or vice versa. Therefore, at the center of the $\lambda/4$ patch, the voltage is zero and the current reaches its maximum. The zero voltage at the center of the $\lambda/4$ patch means a short circuit from the patch to the ground plane. If a shorting pin is physically placed at the center of a $\lambda/4$ microstrip patch, the current and voltage will be basically the same as the ones for a $\lambda/2$ antenna; thus, the antenna will radiate[48]. The resonant frequency of the PIFA antenna is determined by the length of the patch L, the width of the patch W, the width of the shorting pin w_s, and the height of the substrate h. The impedance of the PIFA can be controlled via the distance of the feed to the short pin y_0. The closer the feed is to the shorting pin, the impedance will decrease. The impedance can be increased by moving it farther from the short edge. The PIFA can have it's impedance tuned with this parameter.

The degradation of the antenna performance, due to the proximity of the human

body, can be reduced if the ground plane is modified aiming to confine the electric energy density in the region far from the antenna border[56]. The PIFA design can be reduced to the equation 4.2, where λ is the wavelength in the dielectric. Ths equation can be solved to find the resonant frequency and is expressed as equation 4.3, where v_0 is the free-space speed of light and ε_r is the relative permittivity (dielectric constant) of the substrate.

$$L = -W + w_s + \frac{\lambda}{4} + h \tag{4.2}$$

$$f = \frac{v_0}{4(L + W - w_s - h)\sqrt{\varepsilon_r}} \tag{4.3}$$

4.2.1 PIFA Modeling and Simulation

In Casula and Montisci(2019)[57] the authors presented a design strategy to adequately shape and extend the antenna ground plane, proven to significantly improve the antenna robustness for human body coupling. In this work, they applied this design strategy to a UHF PIFA shown in Figure 4.12.

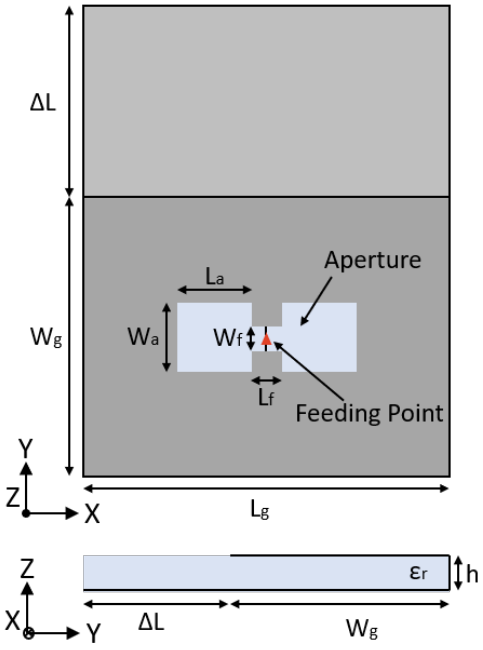

(a) Design layout.

Parameter	Dimensions (mm)
W_g	49
L_g	60
W_a	8
L_a	10
W_f	3
L_f	10
h	4
ε_r	2.08
ΔL	$\frac{\lambda}{10} = 32.5$ (916.25 MHz)

(b) Parameters table.

Figure 4.12: PIFA Antenna layout with design parameters. Adapted from [57].

The antenna robustness was successfully tested trough numerical simulations, considering a human phantom. The simulations were performed using Computer Simulation Technology (CST) Microwave Studio.

This simulation was replicated using the same software and the same human phantom properties. The simulation environment can be seen in Figure 4.13, where the human phantom model is constituted of three layers. The first layer is the skin layer ($\varepsilon_r = 41.32$, $\sigma = 0.855$ S/m @ 900 MHz) and has a thickness of 1.5 mm, followed by the fat layer ($\varepsilon_r = 5.46$, $\sigma = 0.05$ S/m @ 900 MHz) with a thickness of 20 mm, and finally a muscle layer ($\varepsilon_r = 54.97$, $\sigma = 0.934$ S/m @ 900 MHz) with a thickness of 30 mm. Initially the antenna dimensions weren't altered, with the exception of the substrate permittivity(ε_r).

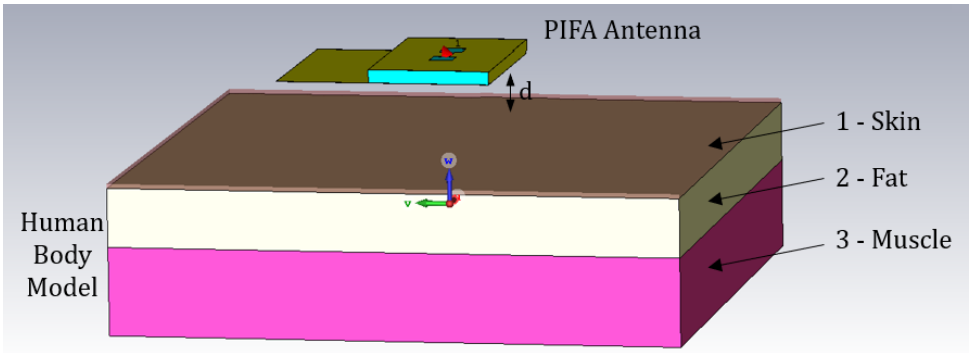

Figure 4.13: PIFA on the phantom model, in the simulation environment.

To verify the PIFA design, a prototype of the antenna was fabricated using the exact same design parameters but with a different substrate than the authors. Since the goal is to achieve a flexible antenna design, Polydimethylsiloxane (PDMS) was chosen as the base elastomer, due to its versatility and mechanical properties. The fabrication process of the flexible substrate, starts with mixing the silicone elastomer base with a curing agent, then cast the pre-cured PDMS mix into a pre fabricated 3D printed mold with the intended dimensions, based of table 4.12b. Then placing the mold in a controlled temperature oven and wait for it to cure. The cast is then removed, resulting in cured stretchable PDMS with the antenna dimensions. For the antenna conductive part, a flexible kapton(50microns) copper(35microns) foil is cut to the appropriate length and the PIFA aperture is cut with an xacto knife. This foil is then glued around the PDMS substrate using silicone based glue(Sil-Poxy^{TM}) and then the coaxial cable is added to complete the fabrication of the PIFA. The

fabricated antenna is visible in Figure 4.14a. It should be mentioned that in the computer simulation the PDMS was modeled with $\varepsilon_r = 2.67$ and $tan\ \delta = 0.37$ [58].

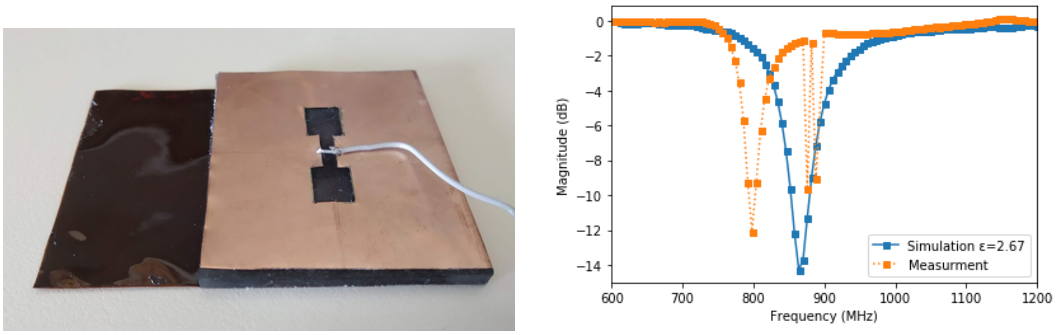

(a) Fabricated Casula2019 PIFA picture. (b) S_{11} Simulation and measurement.

Figure 4.14: Fabricated Casula2019 PIFA characteristics.

After soldering the coaxial cable, the antenna was put through the VNA to evaluate if the resonant frequency matched the simulated one. The S_{11} result is displayed in Figure 4.14b and compared with the simulation. It can be observed that the measured resonant frequency is 70 MHz less than the simulation which was 866 MHz. It is expected to find discrepancy between actual measurements and simulation, but it was concluded that 70 MHz was higher than expected, and considered the computer modeled PDMS permittivity value was inaccurate. Later, a value of $\varepsilon_r = 3$ was found to closely match the measured and simulated value.

Several simulations where conducted to understand the influence of the design parameters, and their effect in respect to the overall antenna behavior. This simulations focused on changing the dielectric height, dielectric permittivity, and distance to the human phantom model. The remaining antenna parameters were adjusted to tune the antenna to the desired impedance and center frequency (915 MHz). Figure 4.15 shows the effect in the antennas reflection coefficient (S_{11}) for a change in the dielectric height. It can be observed that this PIFA maximum dielectric height is around 5 mm as 5.5 mm already shows 10 db reduction in S_{11}. Another effect observable though simulation is a slight increase of the center frequency.

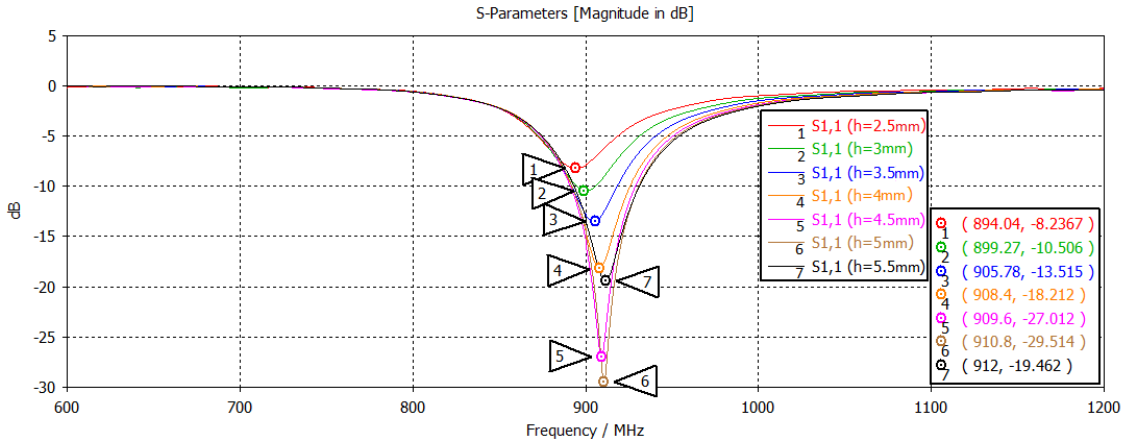

Figure 4.15: Simulation results for varying PDMS ($\varepsilon_r = 2.67$,$tan\ \delta = 0.37$) substrate height.

It can be expected that, increasing the distance(d) of the antenna from the human body, increases the antenna performance, this is observable in Figure 4.16 through simulation the distance was increased by 0.4 mm increments. Such close distance was considered, since the antenna is intended for sub-epidermal placement, for instance placement over a medical gauze, or an elastic band.

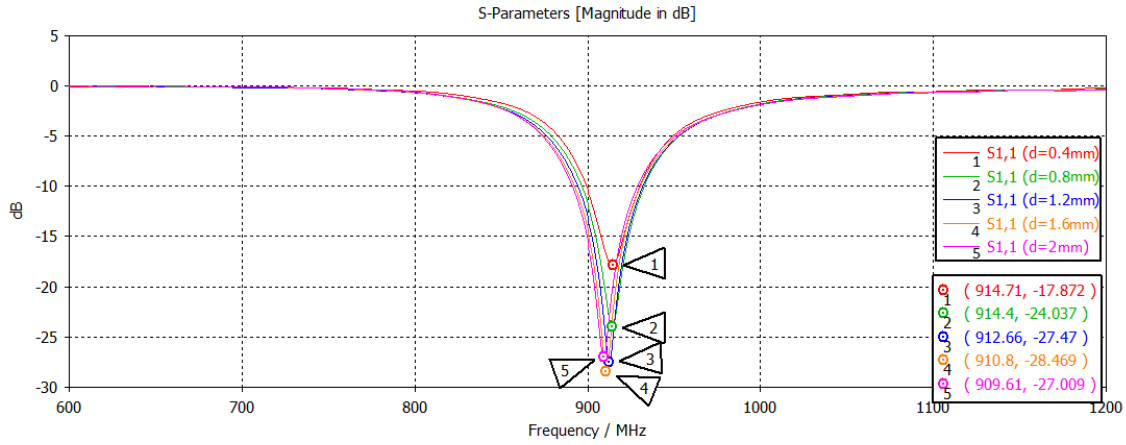

Figure 4.16: Simulation results for varying distance to the human body phantom.

The design parameters in Figure 4.12 were adjusted through simulations to reduce the size of the antenna and to make it more comfortable and unobtrusive as possible for the wearer. The final parameters for the optimized PIFA are listed in Table 4.17b.

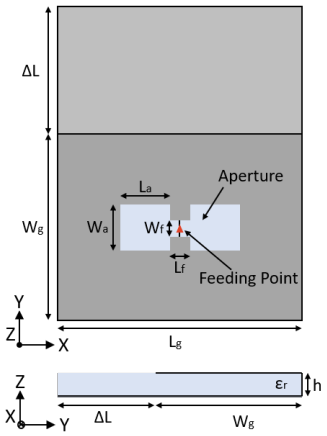

(a)

Parameter	Dimensions (mm)	
	Casula(2019) PIFA	Proposed PIFA
W_g	49	44.3
L_g	60	50
W_a	8	8
L_a	10	8
W_f	3	3
L_f	10	10
h	4	4.5
ε_r	2.08	3
ΔL	32.5 (916.25 MHz)	32.7 (915 MHz)

(b)

Figure 4.17: Proposed PIFA optimized layout, and design parameters comparison with Casula2019 PIFA design.

The resonant frequency was intentionally shifted to 915 MHz as it is the RF harvester optimal operation frequency, this was confirmed through on body measurements with the VNA and the S_{11} plot is observable in Figure 4.18b. Comparing the simulated values, with the measurements acquired with the VNA, the optimized antenna center frequency is 924 MHz which is very close to the simulated value, and the measured return loss was -12.912 dB, which was lower that simulated -22 dB.

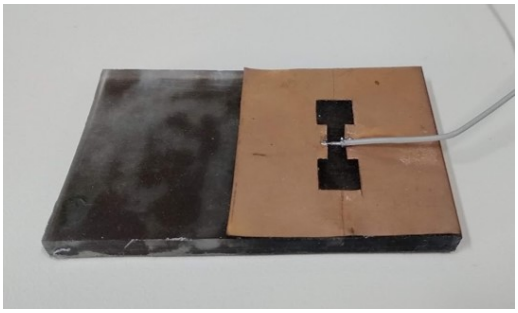

(a)

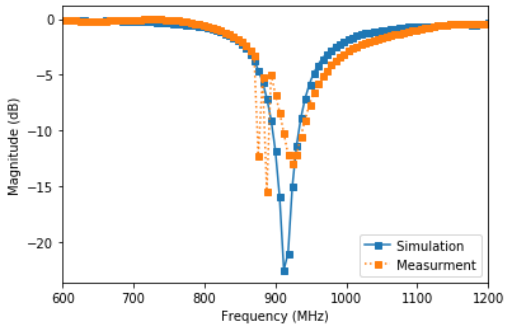

(b)

Figure 4.18: Proposed PIFA characteristics. **a)** Top view and size comparison with Casula2019 PIFA. **b)** Measured and simulated S_{11} of the fabricated antenna.

The differences between our proposed PIFA design and the Casula2019 design can be seen in Figure 4.19. The optimized proposed antenna with the PDMS dielectric is 11.6% smaller in volume than the Casula2019 PIFA. This reduction was achieved with the dielectric change and through simulation iteration of the remaining parameters.

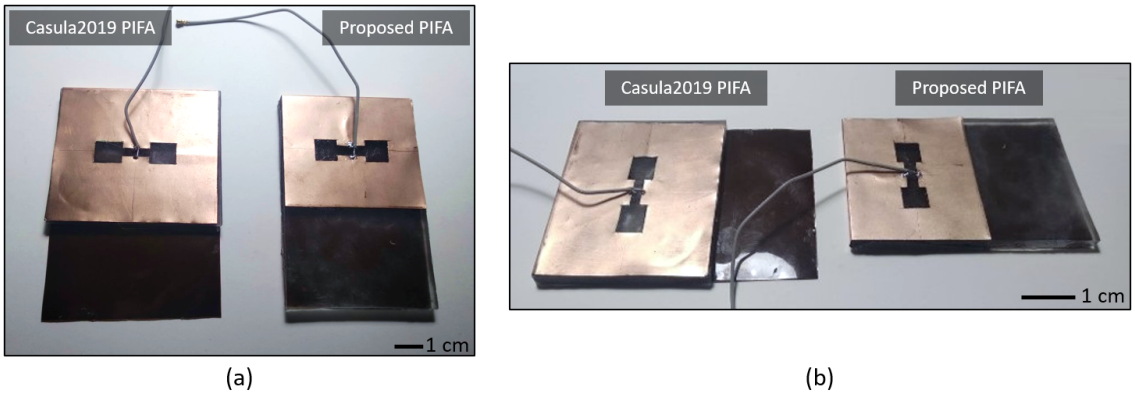

Figure 4.19: Size comparison between the Casula2019 PIFA and the proposed PIFA. **a)** Top view. **b)** Side view.

The radiation pattern defines the strength of the radiated power as a function of the direction away from the antenna, to highlight radiation peaks, and to reveal the efficiency. The directivity of an antenna describes the power received in its peak direction. A high directivity implies that the antenna is more likely to receive signals from a specific direction. The simulated radiation pattern of the optimized PIFA can be observed in Figure 4.20. The resulting simulation shows a gain of 4.63 dBi and about 138 degrees of elevation plane beamwidth(Figure 4.20 d).

After the validation of the proposed PIFA design, the focus was shifted to make the antenna stretchable. Stretchable circuits show promise for many new applications which cannot be fulfilled with rigid antennas. In order to make the proposed optimized PIFA stretchable, the conductive copper foil needs to be replaced by a conductive stretchable material.

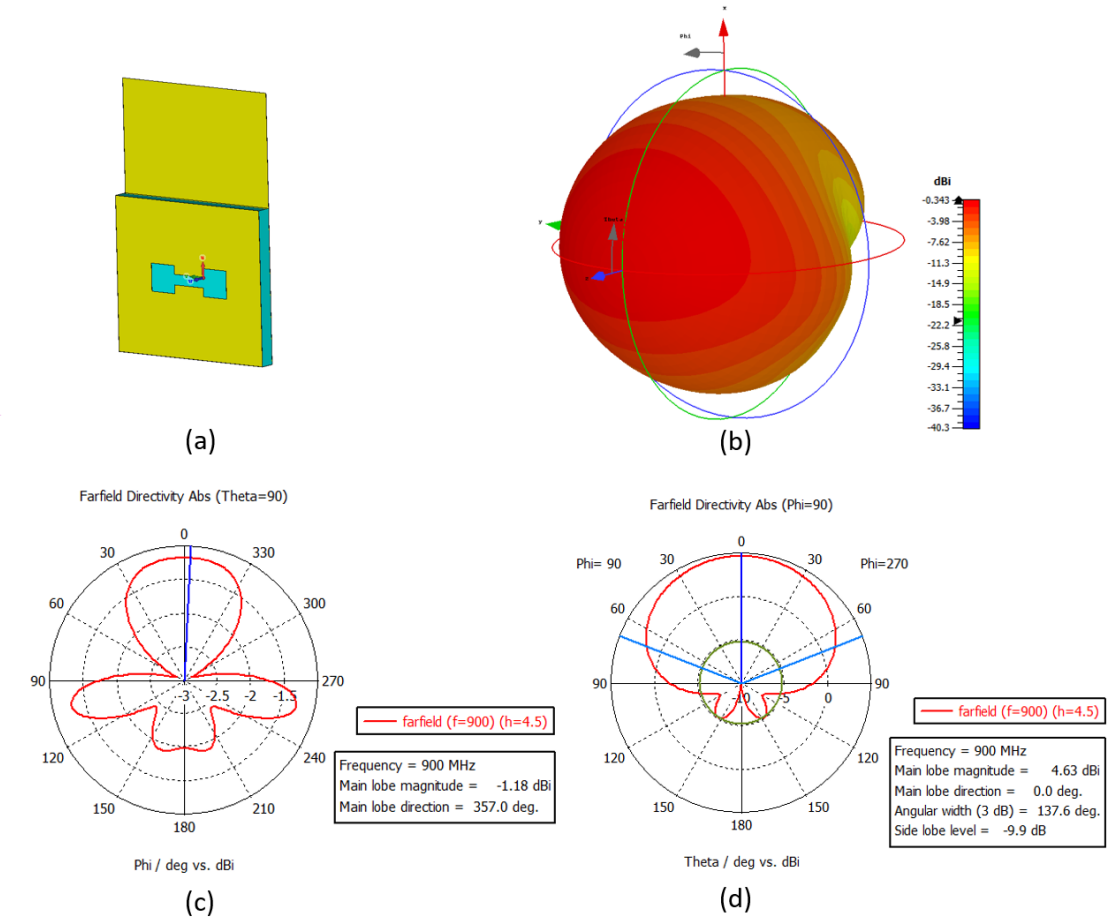

Figure 4.20: Proposed PIFA simulated radiation pattern. **a)** 3D Model. **b)** 3D Radiation Pattern. **c)** Azimuth plane pattern. **d)** Elevation plane pattern.

The process of fabricating this stretchable conductive film is shown in Figure 4.21. At first, a 100μm layer of flexible substrate was spun on top of a wide glass plane, and curing at 60^{o}C after 15 min. Afterward, conductive ink is placed on top of the substrate layer, and spread out using a thin film applicator regulated to 100μm. The ink is left to cure at 60^{o}C for 30 min, to form the conductive film.

This process was repeated several times, while varying the flexible substrate and the conductive ink formulation to find a balance between usability and practicability. There where a few fabrication problems during this process, such as, the ink lacked adhesion to the substrate, the substrate with the ink got lacerated when peeling the films, the conductive ink began to crack while peeling, exposing liquid metal(EGaIn) droplets. The most reliable combination of flexible substrate and conductive ink, for accessible fabrication ended up being Styrene-isoprene block copolymers (SIS) for the substrate, and the conductive stretchable ink was by mixing a high surface

area Silver (Ag) flakes 41-071 (Technic) and TPU.

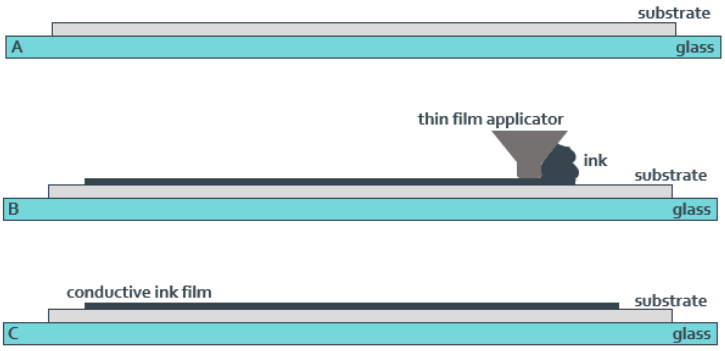

Figure 4.21: Schematic of the stretchable conductive layer fabrication process. **A**: The SIS layer is cured on top of a glass in order to cure uniformly. **B**: Ink is poured over the substrate and spread using a thin film applicator to ensure layer height. **C**: The ink is cured to form the conductive film.

Figure 4.22: Stretchable proposed PIFA fabrication process. **i**: The stretchable conductive ink film is peeled of the glass, **ii**: then is folded over the substrate, and the excess is removed . **iii**: A previously cut stencil is placed on the top plane, and the aperture is cut an x-acto knife. **iv**: The coaxial cable terminals are then connected to the film with small drops of the conductive ink.

In Figure 4.22 the second part of the process is demonstrated, where the 200 μm conductive double layer is warped around the 4.5 mm height, PDMS substrate, and then cut to the specified dimensions stated in Table 4.17b. The resulting stretchable Ag PIFA is seen on Figure 4.23a together with the simulated and measured S_{11} parameters. The Ag PIFA can withstand mechanical deformations as shown in Figure 4.24. The measured center frequency is 916 MHz with 1.523 VSWR and -13.661 dB return loss.

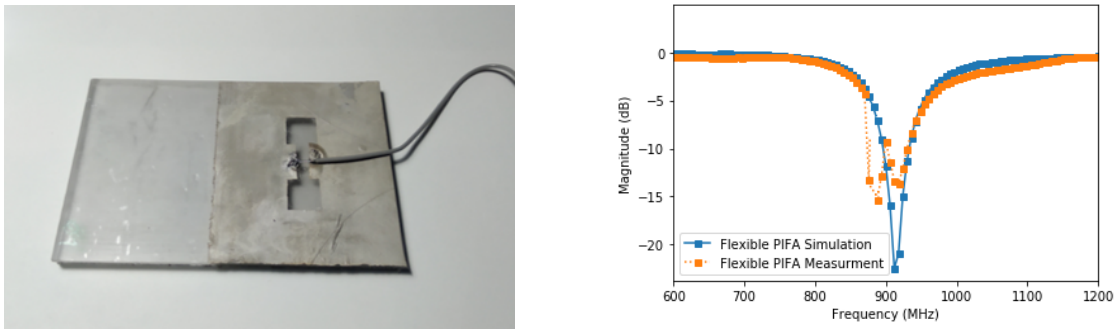

(a) (b)

Figure 4.23: Stretchable proposed Ag ink PIFA. **a)** Top view. **b)** Measured and simulated S_{11} of the fabricated antenna.

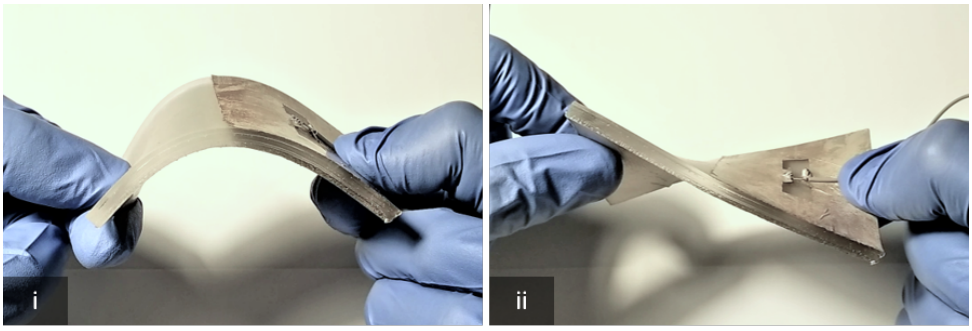

Figure 4.24: Stretchable proposed Ag PIFA being deformed. **i**: Bending and, **ii**: twisting.

4.2.2 Chapter Summary

In this chapter we've replicated the 1 dBi PCB antenna design from Powercast in a flexible elastomer, characterized it in respect of, center frequency, return loss and VSWR using the Vector Network Analyzer (VNA) device, and compared the total energy harvested when using the rigid PCB antenna and the flexible antenna. Due to unsatisfactory results, another antenna design was considered, the folded dipole. This antenna design was fabricated using several substrates, from rigid to stretchable materials, where each of the resulting antennas was classified and evaluated relative to the amount of energy the system could harvest. Some of the folded dipole antennas showed promising results when evaluated on the free space medium, but when the antenna was placed over the skin of a human test subject, the amount of energy it rectified was bellow expectations.

Consequent to this, the focus shifted to an antenna design that showed robustness

to the human body, the Planar Inverted-F Antenna (PIFA). To model this antenna we used a computer assisted simulation(CST Microwave Studio), in the simulation environment we included a human body phantom to optimize the antenna design and to tune the center frequency to the harvester specifications. To ascertain the viability of using the PIFA design, we fabricated this antenna using Polydimethylsiloxane (PDMS) for the dielectric material, and copper foil. Through VNA measurements, we confirmed the design showed robustness when in close poximity with the human body, and proceeded to fabricate a flexible version of the antenna. In the next chapter, the experimental results of the PIFA design will be discussed, in respect of RF energy harvesting.

Chapter 5

Case studies

In this chapter we will analyze the total amount of power harvested for the last antenna design(PIFA). The experimental results of each PIFA iteration will be discussed, as well as the overall harvester system performance.

5.1 PIFA Experimental results

This section will answer the question, how much of an improvement was gained for each PIFA design iteration, and how does it reflect on the overall system harvested power. The evaluation will cover two different conditions, in the first one, the antenna is placed on free space while being subject to a noisy environment. The second one, the antenna is evaluated while being placed on the human body and still being subject to a similar noisy environment. This experiment setup is represented in Figure 5.1.

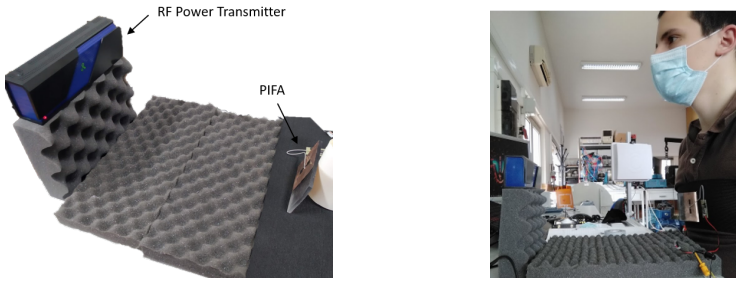

(a) (b)

Figure 5.1: Experiment setup. Antenna is placed at a fixed distance, **a)** on free space, **b)** on a subject chest.

The experiments will follow the methodology of evaluating the time it takes to charge a 35 mF supercapacitor with the harvester system. This methodology was already used and described in subsection 4.1. Table 5.1, summarizes the antenna parameters obtained with the VNA of the three fabricated PIFAs.

Parameters	Casula2019 PIFA	Proposed PIFA	Proposed Stretchable PIFA
Frequency	798 MHz	924 MHz	916 MHz
Return loss	-12.082 dB	-12.912 dB	-13.66 dB
VSWR	1.663	1.585	1.523
Impedance	$54.5 - j26.4\Omega$	$57.6 + j23.7\Omega$	$40.2 + j16.3\Omega$

Table 5.1: Summarized VNA measurements for the three fabricated PIFAs detailed in section 4.2.1.

The first experiment, exhibits the comparison of the Casula and Montisci(2019)[57] PIFA in the free space setup and the on body setup. From the plot in Figure 5.2 it is observable that the antenna shows low attenuation when placed on the body, which makes this design a suitable candidate for our application. Although the harvested power is bellow the requirements. The antenna on free space delivered 0.6 mW, and the on body setup 0.5 mW. This result was expected , due to the center frequency of the antenna not being in the optimal intended range of the P1110B harvester and the M6E-Nano RFID module Tx frequency(915 MHz).

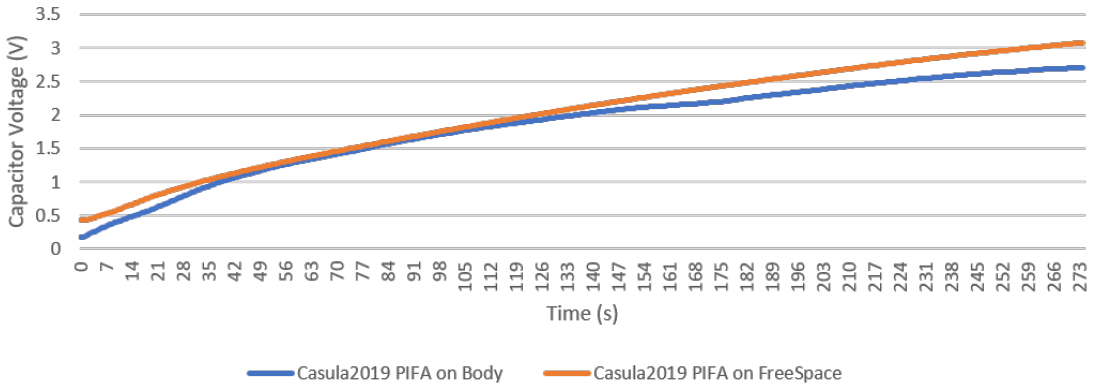

Figure 5.2: RF Harvester supercapacitor charge time, comparison between free space and on body placement of the Casula2019 PIFA. Experiment was done with the antenna at a fixed distance of 30 cm from the Tx.

The previous result confirms the PIFA robustness to the human body, and motivated the adjustment of the PIFA design parameters, with the aim to tune the antenna to a specific frequency. The operating frequency of the RFID M6E-Nano Tx can be configured from 859-873 Mhz and 915-930 Mhz. The P1110B datasheet states that the optimal frequency its 915 Mhz, therefore shifting the antenna frequency to 915 Mhz will improve the overall performance of the harvester system. The simulation process of the optimization were already discussed previously, now the harvested power results and depicted in Figure 5.3 where a vast improvement is shown on the harvester performance. The plot reveals the difference between the Casula2019 version and the proposed version of the PIFA. For the proposed optimized PIFA on body, the harvester reaches saturation(4.2 V) within 125 seconds, which amounts to 2.572 mW of power, approximately 5 times more than the Casula2019 PIFA design.

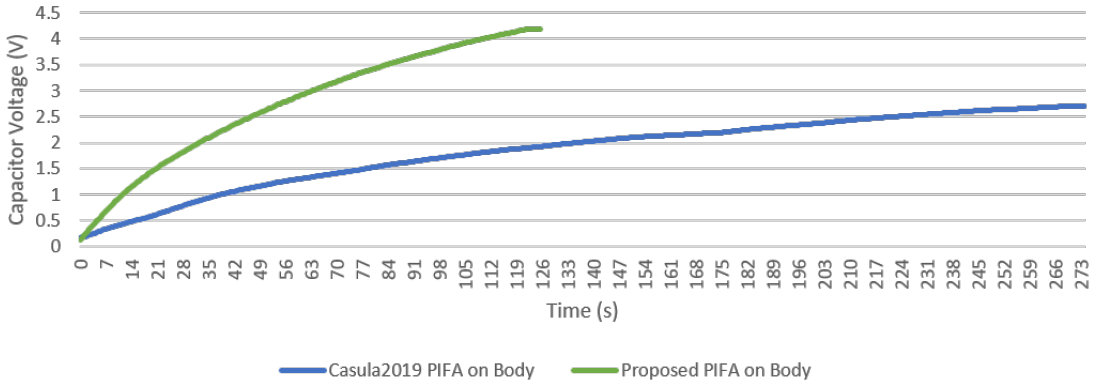

Figure 5.3: RF Harvester supercapacitor charge time, comparison between Casula2019 and the proposed PIFA. Data was acquired with both antennas at 30 cm from the Tx, on a human subject body.

Following the success of the proposed Copper (Cu) PIFA, let us now compare the performance against the stretchable conductive Silver (Ag) ink PIFA. In Figure 5.4 plot, we observe that both antennas perform very similar, and this result is consistent with the VNA measurements summarized in Table 5.1, the Ag antenna slightly outperforms the Cu one, harvesting 3.36 mW and 3.18 mW respectively, on the free space medium.

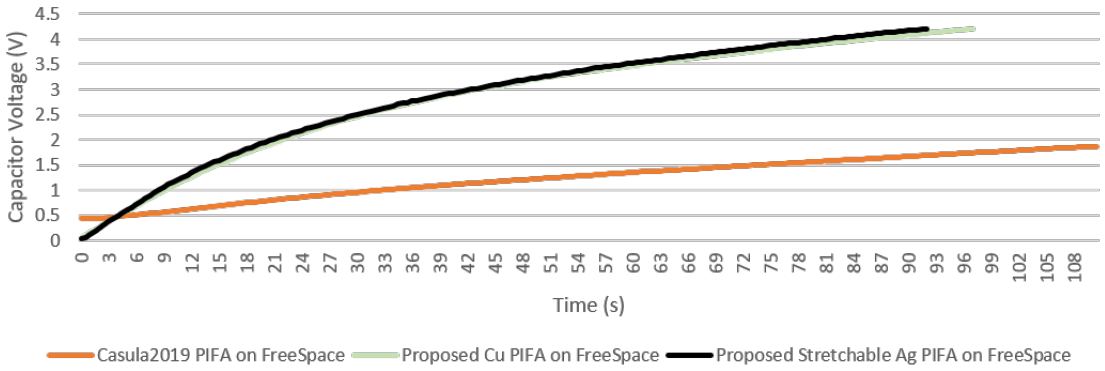

Figure 5.4: Supercapacitor charge time comparison between Casula2019 PIFA, the proposed Cu PIFA and the stretchable Ag conductive ink PIFA. Data was acquired with both antennas at 30 cm from the Tx, on free space.

With the successful optimization, and fabrication of the stretchable PIFA, the focus shifted to find ways of increasing the amount of power harvested. The approach followed was increasing the RF power transmitted to the harvester system, for this we used two transmitters, the M6E-Nano with the external antenna, and the Powercast Powerspot transmitter. The experiment setup is seen in Figure 5.5.

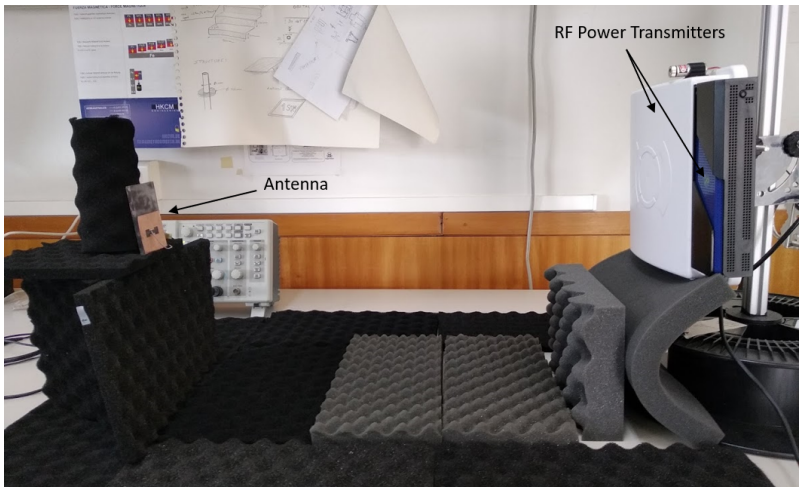

Figure 5.5: Dual RF transmitter experimental setup.

From Figure 5.6 it can be observed the effects of having both transmitters active at the same time, as well as a comparison of having just one of them. The RF harvester system charges the capacitor in under 60 seconds, which increased the harvested power to 5.15 mW, that doubled the amount of power the harvest system was able to supply with just one Tx antenna. The charging time of the capacitor

was also cut by approximately half. This seems very promising, as the harvested power was the sum of both systems, without any noticeable loss. This is a subject of the future work to discover the limits of this approach, i.e. how many antennas can be added with this linear increase on the harvested energy.

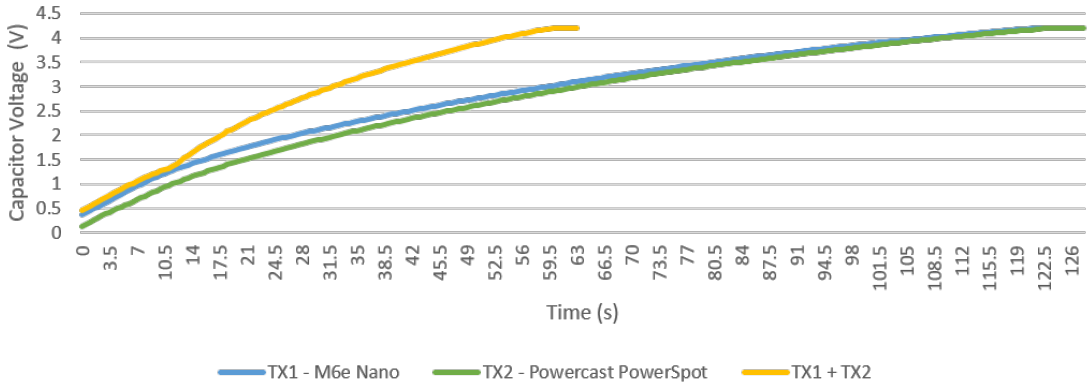

Figure 5.6: Supercapacitor charge time while using each RF transmitters individually, and both at the same time. Data was acquired with the antenna at 30 cm from the Tx, on free space.

Following the parallel scaling of the Tx setup, we applied the same concept, for the Rx part of the harvester system. That is, to add additional receiver antennas, for a single transmitter, and measure the harvested energy. For this, two additional PIFA antennas had to be fabricated to evaluate the feasibility of this approach. The proposed Cu PIFA were easier and faster to fabricate, so we used those. From theoretical background, adding two antennas in parallel would not work, because it would half the total impedance of the port, and split the power between them. So the valid approach was to have one harvester for each fabricated antenna, and connecting the output in parallel.

In Figure 5.7 is shown a picture of the three P1110B harvesters with the three fabricated antennas, and the supercapacitor used for the experiments. The decision for choosing the number of antennas, was biased on a possible application of this system. The concept devised of, having an elastic band warped around a patient chest for ECG acquisition. With this in consideration, the average male adult has a chest width of 40 cm[59], and therefore we decided to occupy half of the belt space for placing the harvesting antennas to ensure proper separation between them, which ended up being three antennas, with 2.5 cm of horizontal separation between them,

making the overall footprint of the chest band 20 cm wide by about 4.5 mm thick, due to the PIFAs structure.

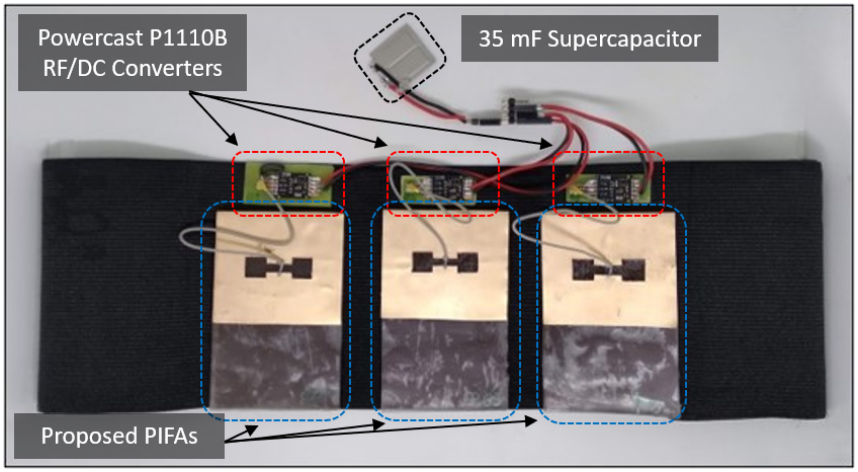

Figure 5.7: Triple RF harvester configuration.

The result of using the triple harvester configuration is depicted in Figure 5.8, in which it is observable 2.7 times improvement over using a single antenna. The triple PIFA harvester system configuration is able to produce 10 mW of power for a distance of 30 cm, with just one transmitter. This shows that there is some linearity with the increased number of harvesters and antennas.

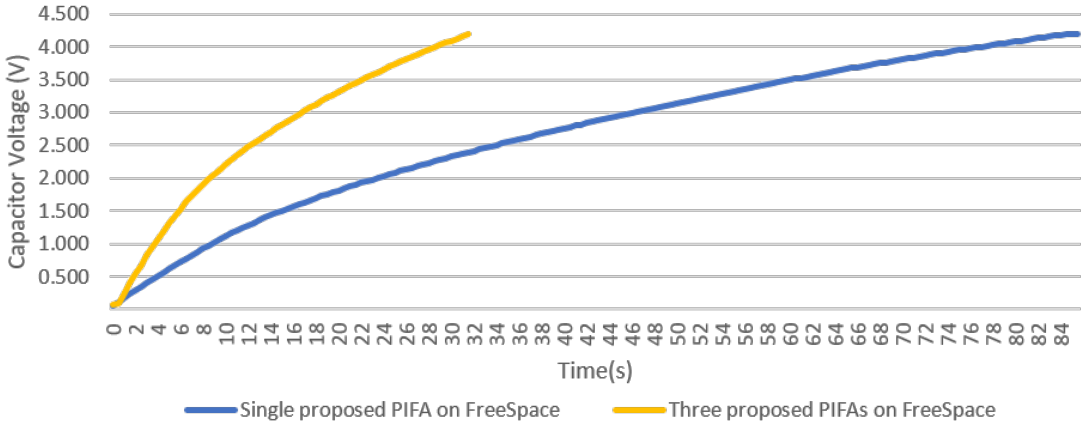

Figure 5.8: Comparison between, a single RF harvester with the proposed PIFA and three RF harvesters in parallel with proposed PIFAs. Data was acquired with all antennas at 30 cm, on free space.

In Figure 5.9 a comparison of the triple harvester configuration is shown with the harvester chest band placed on free space an on the human body. As previously

mentioned, the PIFA shows robustness when placed on the human body, but it is observable an amplified attenuation for the triple configuration when its placed on the human body. Still, the results look promising, in Figure 5.10, we can see the amount of power harvested for this configuration, over a distance span of 1.1 meters. It can be extracted from the data table in the plot, the amount of power the triple harvester configuration can produce at a certain distance from the transmitter. This graph was created from charging the suppercapacitor at every 10 cm and calculating the amount of power the system harvested based on the amount of time it took to charge the supercapacitor. The measurements started at 20 cm to avoid damaging the PB1110 harvester module.

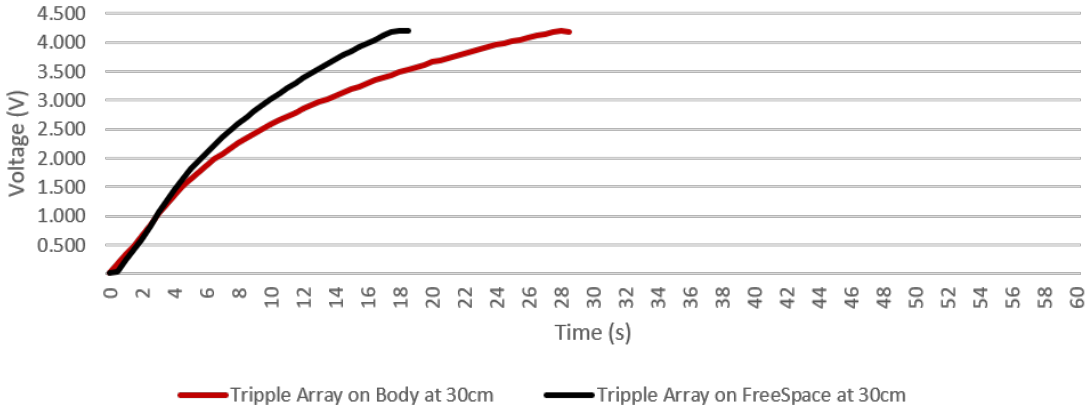

Figure 5.9: Supercapacitor charge time comparison between the triple array placed on body and on free space at 30 cm . The data was acquired while using two RF Tx.

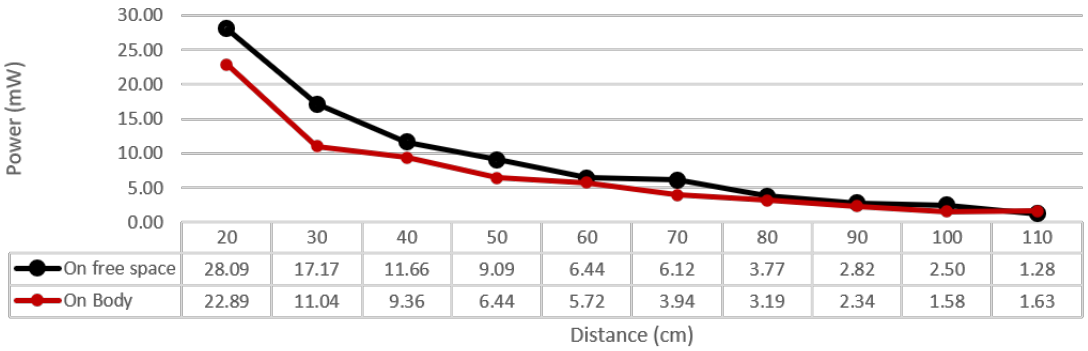

Figure 5.10: Total amount of power harvested over distance, while using three harvesters with three proposed Cu PIFAs, using two RF Txs.

5.2 Feasibility results and application

At this stage, it is important to revisit the motivation behind the feasibility analysis. The goal of this dissertation is to investigate the practicability of far-field WPT systems for biomedical applications. This work is a contribution towards the development of wireless biomonitoring stickers. This stickers can be used to identify physiological and emotional responses through the collection of diverse data, such as heart, muscle and brain activities (ECG/EMG/EEG respectively).

5.2.1 ECG acquisition device.

For the practical application of this work, we used a commercially available ECG acquisition device for validation of the WPT system. The Movesense ECG device is slightly bigger than two euro coin size and contains multiple sensors for measuring motion and human physiology. Movesense provides a mobile phone application that enables server-client connection for communication over wireless Bluetooth Low Energy (BLE) and API uses Representational State Transfer (REST) type format for (service) messages between apps. REST technology API is based on HTTP protocol.

Figure 5.11: Movesense wearable sensor platform by Suunto.

The device is able to store measurements in non-volatile memory, hence reducing need to keep BLE wireless connection powered unnecessarily and saving battery life at the same time. Typically the device is powered by a coin cell battery, but in this case the battery will be removed, and the Movesense^{TM} will be directly powered by the RF harvester. The Movesense^{TM} seen in Figure 5.11 uses nRF52832 MCU from Nordic Semiconductors. The nRF52832 is an advanced low-power SoC including a radio for BLE4.0, 2.4GHz communication. Multiprotocol

radio has hardware support for Bluetooth 5 and is compatible with ANT protocol. The nRF52832 SoC is designed for low-power applications and it can be used with a supply voltage from 1.7 to 3.6 volts. The Movesesense^{TM} uses low power components to enable low power usage which makes it suitable for our harvesting system. The following list describes the electronic components included in this tiny device.

- Accelerometer and gyroscope combo LSM6DSL from STMicroelectronics;
- Magnetometer LIS3MDL from STMicroelectronics;
- Temperature sensor TMP112 from Texas Instruments;
- Heart rate sensor MAX30003 from Maxim Integrated;

In order to study the device energy requirements, a power consumption analysis was conducted. The device was attached to the chest of a human subject, and the phone application was used to request the sensors data. For the Heart rate and ECG sensor subscription, the average power consumption obtained was $5.86mW$, peaking at $6.2mW$ when the status LED was active. Results are listed in Table 5.2.

Subscribed Sensor	**Voltage (V)**	**Current (mA)**	**Power (mW)**
Idle	2.6663	1.87	4.980
ECG	2.665	2.20	5.841
BPM	2.651	2.21	5.859
Accelerometer	2.656	2.07	5.498
LED	2.696	2.30	6.201
Multiple	2.636	2.06	5.430
Subscriptions	2.624	2.45	6.429
(IMU 3axis,6axis)	2.613	3.40	8.884

Table 5.2: Measured power consumption of the Movesense^{TM} device.

5.2.2 WPT Biomonitoring prototype

To finally validate the RF harvester system, that was developed throughout this work, we created a prototype, wirelessly powered ECG monitoring chest-band, as a possible biomonitoring application of the RF WPT system. The chest band depicted in Figure 5.12a consists of three flexible Ag PIFAs described in subsection 4.2.1, and and three P1110B RF/DC harvester modules. The output of each module is connected in parallel to a 35 mF supercapacitor which is connected to the Movesense^{TM} ECG device, as shown in Fig 5.12b. The supercapacitor is used as a backup storage device, that can store the harvested energy when the biomonitoring system is not consuming the whole harvested energy, and use the stored energy for cases when a higher consumption may be necessary, or when the antenna path is blocked.

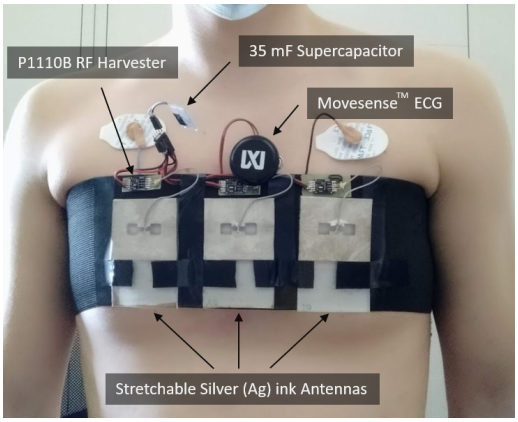

(a) Prototype band on subject's chest.

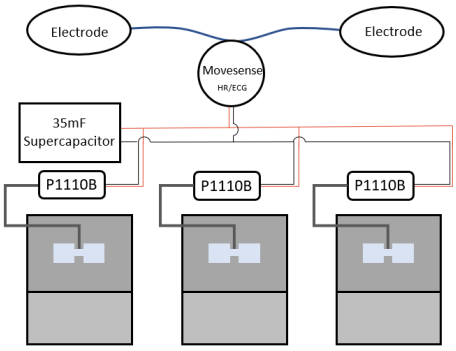

(b) Prototype chest-band schematic.

Figure 5.12: Prototype WPT chest-band with Movesense^{TM} ECG device.

It should be mentioned that, although the Movesense^{TM} device uses low consumption sensors and power saving algorithms, it requires a higher power to initialize. Consequently the device needs to be either closer to the RF source or manually powered after a certain threshold voltage(at super capacitor output) is reached. Obviously, the energy supplied by the RF harvester over time should be greater than the energy consumed by the device, to ensure long term operation. In Figure 5.13a we can see the ECG chest-band placed on a human test subject, as well as the RF WPT system. In this experimental setup, we were able to fully power the Movesense ECG device without the use of a battery.

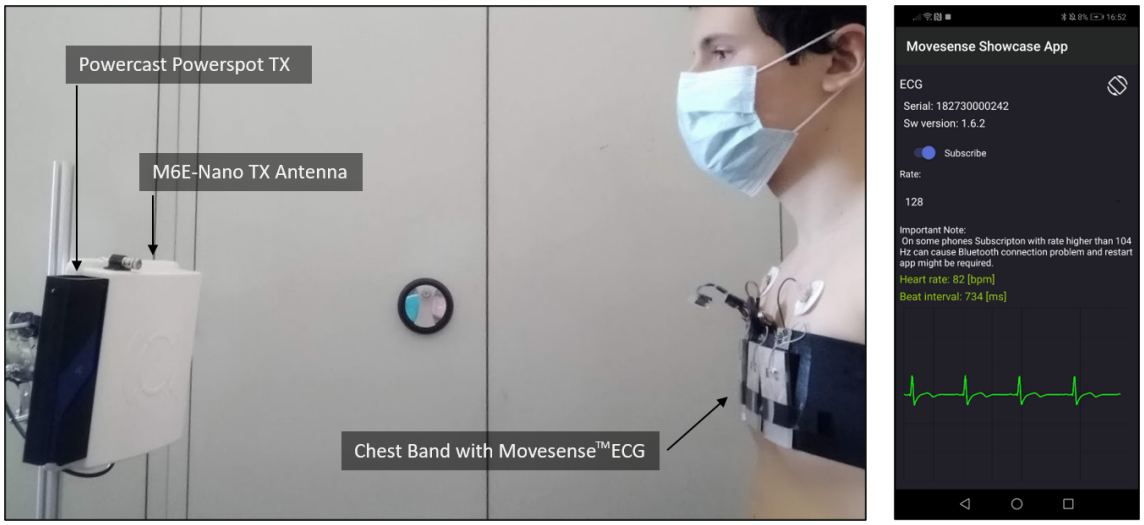

Figure 5.13: Application of the WPT chest-band. **a**) Experimental setup. **b**) Movesense^{TM} Phone APP, showing ECG data.

The graph in Figure 5.14 shows the voltage at the supercapacitor output for this experiment. Experimental methodology and graph analysis: The belt was attached to the subject, and the subject was placed at 30 cm from the RF transmitters. The transmitters were powered on, charging the supercapacitor. When voltage saturation was reached at the capacitor output, the Movesense device was connected to the harvesting system($t = 29s$). The voltage drops for a few seconds, as the device initializes, and then the capacitor continues to charge since the harvested energy is greater than the power consumption at that distance. At $t = 50s$ the subject starts slowly moving away from the transmitter and stops at a distance of 50 cm($t = 58s$). The harvested energy is still greater than the power consumption, so the subject moves back away from the transmitter to 55 cm and stops($t = 70s$). The slope from $t = 70s$ to $t = 77s$ shows that the system is still charging the supercapacitor but at a much slower rate. The subject steps closer to the Tx, were we see the supercapacitor reach saturation.

At $t = 136s$ a new experiment is done, the subject blocks the RF path on purpose for about 6 seconds and repeats this process four more times at a distance of 50 cm. At $t = 237s$ the subject takes a step back to about 60 cm away from the Tx, and blocks the RF path again at $t = 245s$.

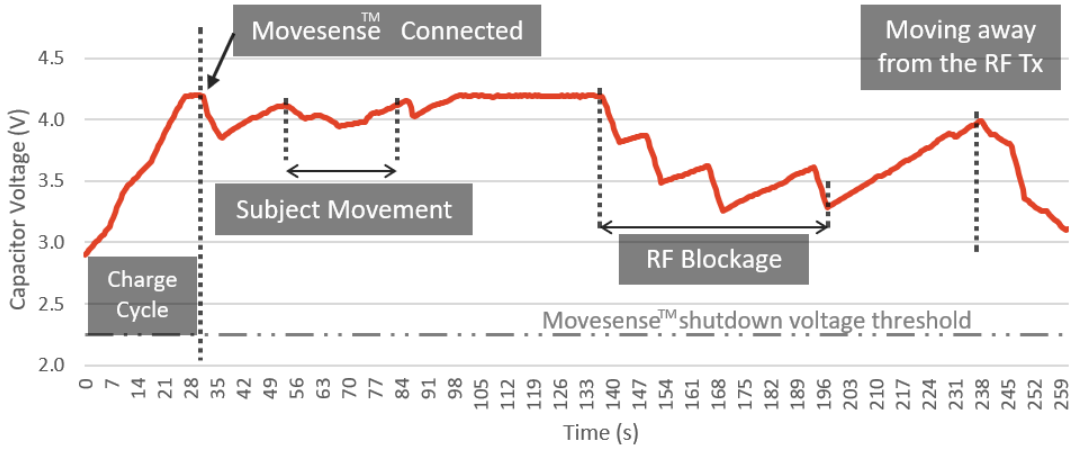

Figure 5.14: Case study, chest-band output voltage, for a controlled experiment on human subject. Measurements included two Txs.

From the previous experiments, we can gather that the RF WPT system is very sensible to distance changes and blockage of the RF waves. And that although the system works, it might not be viable to use it without some additional form of storing energy for larger periods of time. For the chest-band, the 35 mF supercapacitor is capable of supplying power to the Movesense ECG device for about 30 seconds, thus a ultra-thin flexible battery or a stretchable battery would be the ideal for electronic bio stickers.

5.2.3 Chapter Summary

To summarize, the PIFA efficiency was proven to be minimally affected when it is in close proximity with the human body. Our proposed optimized design of the PIFA, showed to be 5 times better in terms of harvested power, than the replicated Casula2019 PIFA with PDMS dielectric. The fabricated stretchable Ag ink proposed PIFA, demonstrated to be on par with the non stretchable Cu proposed PIFA, slightly outperforming it, in respect of the harvested power by 5.6%.

Afterwards, we evaluated how the harvested power relates to the effect of using two Transmitter (Tx) units. This doubled the harvested power amount. A similar experiment was done, to see if increasing the amount of harvesters also showed linearity in respect of harvested power. To do this we fabricated two more antennas and arranged them in a triple harvester with antenna configuration(Figure 5.7). This configuration showed a 2.7 times increase when compared with using just a

single antenna/harvester combo. Then we tested the triple harvester configuration on free space and on the human body, using to RF transmitters at several distances, and obtained the values in Table 5.3. Furthermore, we created a prototype wireless powered biomonitoring chest-band, that can acquire ECG data without the need of a battery. The ECG chest-band wast tested on a human subject and was able to power the Movesense^{TM} ECG acquisition device, that has a measured power consumption of around 6 mW, at a distance of 55 cm.

Distance (cm)	**On FreeSpace Medium**	**On Human Body (Chest)**
20 cm	28.09 mW	22.89 mW
30 cm	17.17 mW	11.04 mW
40 cm	11.66 mW	9.36 mW
50 cm	9.09 mW	6.44 mW
60 cm	6.44 mW	5.72 mW
70 cm	6.12 mW	3.94 mW
80 cm	3.77 mW	3.19 mW
90 cm	2.82 mW	2.34 mW
100 cm	2.50 mW	1.58 mW
110 cm	1.28 mW	1.63 mW

Table 5.3: Harvested power over distance, on free space and on human body, for the triple harvester configuration, using two Txs.

Chapter 6

Conclusion

In this work, we developed and characterized several antennas for WPT applications. We used flexible substrates together with conductive LM alloy ink to fabricate flexible antennas. These types of antennas provide the needed mechanical flexibility for epidermal WPT biomonitoring applications. It was also proven that introducing a large size ground plane to the antenna significantly reduces the negative effect caused by the human skin in terms of antenna performance.

According to the obtained results and subsequent discussion, we could answer all of the research questions listed in chapter 1. We've compared PCB antennas with stretchable antennas, observed how the antenna geometry affected the harvested energy of the system, and showed how the human body negatively influences antenna performance. Finally, we proved the viability of using RF WPT for biomonitoring applications, by creating a wirelessly powered ECG monitoring chest-band. The prototype chest-band uses three of our proposed stretchable PIFA antennas, and three P1110B commercially available RF harvesters(70% efficiency) and a Movesense^{TM} ECG monitoring device.

The developed wirelessly powered ECG monitoring chest band eliminates the need for wires and batteries, and it is reasonable to conclude that the RF WPT system is feasible. The far-field WPT has proven advantages over near field, one being the lack of coupling problems, and the increased power transmitting distance. A maximum power of 3.36 mW at 30 cm was achieved in a relatively noisy environment for a single Rx antenna and harvester while using one RF Tx at 27 dBm. Which is an acceptable power level for several LoS patches. However, 30 cm is too low

distance between the transmitter and the biomonitoring device for most biomedical applications. So, we scaled the system to three Rx antennas and three harvesters and the maximum power for the same 30 cm distance was increased to 10 mW. Introducing another RF Tx(3W) increased the total harvested power to 17.17 mW. It should be noted that, these metrics are in reference to free space medium. For the ECG chest-band on a human test subject, the maximum achieved distance for continuous operation was 55 cm while using two RF Tx.

The practical limitations of a WPT system, include RF losses, antenna impedance mismatch, RF energy distribution in realistic environments, government regulations, rectifier efficiency and Rx antennas size restrictions. In our proposed antenna design we increased the antenna ground plane to minimize the RF losses caused by the human body, unfortunately this resulted in a relatively thick antenna structure, which leads to a less versatile antenna, and it can negatively affect the user experience.

6.1 Future work

In sum, the work presented in this dissertation provides insight regarding the benefits and shortcomings of using WPT for medical devices. The majority of the work, focused on the development of an antenna, that could maximize the harvested power while being in close contact to the human body. Further improvements could be made to miniaturize the antenna, making it more comfortable for the wearer. Using an elastomer with a lower loss tangent could further improve the antenna efficiency, thus also contributing for miniaturization.

Furthermore, a future development goal could be to utilize the existing WPT RF system for simultaneous wireless data and energy transfer. By using the RFID to transfer data instead of conventional BT methods, the power consumption of biomonitoring devices could be reduced. That directly correlates to an increase in distance for a WPT system.

Bibliography

[1] Pedro Alhais Lopes, Davide Vaz Gomes, Daniel Green Marques, Pedro Faia, Joana Góis, Tatiana F. Patrício, Jorge Coelho, Arménio Serra, Aníbal T. de Almeida, Carmel Majidi, and Mahmoud Tavakoli. Soft Bioelectronic Stickers: Selection and Evaluation of Skin-Interfacing Electrodes. *Advanced Healthcare Materials*, 8(15):1–11, 2019.

[2] P. Salvo, A. Pingitore, A. Barbini, and F. Di Francesco. A wearable sweat rate sensor to monitor the athletes' performance during training. *Science and Sports*, 33(2):e51–e58, 2018.

[3] Sumit Majumder, Tapas Mondal, and M. Jamal Deen. Wearable sensors for remote health monitoring. *Sensors (Switzerland)*, 17(1), 2017.

[4] Theresa Roland, Sebastian Amsüss, Michael Friedrich Russold, Christoph Wolf, and Werner Baumgartner. Capacitive Sensing of Surface EMG for Upper Limb Prostheses Control. *Procedia Engineering*, 168:155–158, 2016.

[5] Alexandros Pantelopoulos and Nikolaos G. Bourbakis. A survey on wearable sensor-based systems for health monitoring and prognosis. *IEEE Transactions on Systems, Man and Cybernetics Part C: Applications and Reviews*, 40(1):1–12, 2010.

[6] Eric Y Chow, Arthur L Chlebowski, Student Member, Sudipto Chakraborty, William J Chappell, and Pedro P Irazoqui. Fully Wireless Implantable Cardiovascular Pressure Monitor Integrated with a Medical Stent. 57(6):1487–1496, 2010.

[7] Tamer Elfaramawy, Cheikh Latyr Fall, Student Member, and Martin Morissette. Wireless Respiratory Monitoring and Coughing Detection Using a Wearable Patch Sensor Network. pages 197–200, 2017.

[8] Karandeep Malhi, Subhas Chandra Mukhopadhyay, Julia Schnepper, Mathias Haefke, and Hartmut Ewald. A zigbee-based wearable physiological parameters monitoring system. *IEEE Sensors Journal*, 12(3):423–430, 2012.

[9] Takuji Suzuki, Hirokazu Tanaka, Shigenobu Minami, Hiroshi Yamada, and Takashi Miyata. Wearable wireless vital monitoring technology for smart health care. *International Symposium on Medical Information and Communication Technology, ISMICT*, pages 1–4, 2013.

[10] Zhibo Pang, Lirong Zheng, Junzhe Tian, Sharon Kao-Walter, Elena Dubrova, and Qiang Chen. Design of a terminal solution for integration of in-home health care devices and services towards the Internet-of-Things. *Enterprise Information Systems*, 9(1):86–116, 2015.

[11] Ha Uk Chung, Bong Hoon Kim, Jong Yoon Lee, Jungyup Lee, Zhaoqian Xie, Erin M. Ibler, Kun Hyuck Lee, Anthony Banks, Ji Yoon Jeong, Jongwon Kim, Christopher Ogle, Dominic Grande, Yongjoon Yu, Hokyung Jang, Pourya Assem, Dennis Ryu, Jean Won Kwak, Myeong Namkoong, Jun Bin Park, Yechan Lee, Do Hoon Kim, Arin Ryu, Jaeseok Jeong, Kevin You, Bowen Ji, Zhuangjian Liu, Qingze Huo, Xue Feng, Yujun Deng, Yeshou Xu, Kyung In Jang, Jeonghyun Kim, Yihui Zhang, Roozbeh Ghaffari, Casey M. Rand, Molly Schau, Aaron Hamvas, Debra E. Weese-Mayer, Yonggang Huang, Seung Min Lee, Chi Hwan Lee, Naresh R. Shanbhag, Amy S. Paller, Shuai Xu, and John A. Rogers. Binodal, wireless epidermal electronic systems with in-sensor analytics for neonatal intensive care. *Science*, 363(6430):0–13, 2019.

[12] Ding Bing Lin, Tse Hsuan Wang, and Fu Jung Chen. Wireless power transfer via RFID technology for wearable device applications. *2015 IEEE MTT-S International Microwave Workshop Series on RF and Wireless Technologies for Biomedical and Healthcare Applications, IMWS-BIO 2015 - Proceedings*, pages 210–211, 2015.

[13] Yuhao Liu, Matt Pharr, and Giovanni Antonio Salvatore. Lab-on-Skin: A Review of Flexible and Stretchable Electronics for Wearable Health Monitoring. *ACS Nano*, 11(10):9614–9635, 2017.

[14] Guang-Zhong Yang. Introduction. In *Implantable Sensors and Systems*, pages 1–17. Springer International Publishing, Cham, 2018.

[15] Dae Hyeong Kim, Nanshu Lu, Rui Ma, Yun Soung Kim, Rak Hwan Kim, Shuodao Wang, Jian Wu, Sang Min Won, Hu Tao, Ahmad Islam, Ki Jun Yu, Tae Il Kim, Raeed Chowdhury, Ming Ying, Lizhi Xu, Ming Li, Hyun Joong Chung, Hohyun Keum, Martin McCormick, Ping Liu, Yong Wei Zhang, Fiorenzo G. Omenetto, Yonggang Huang, Todd Coleman, and John A. Rogers. Epidermal electronics. *Science*, 333(6044):838–843, 2011.

[16] IDTechEx. Rfid forecasts, players and opportunities 2019-2029, 2019.

[17] IDTechEx. Flexible, printed and organic electronics 2020-2030: Forecasts, technologies, markets, 2020.

[18] Istitute of Systems and Universidade de Coimbra Robotics. Wow - wireless biomonitoring stickers and smart bed architecture: towards untethered patients, 2020.

[19] N Ravishankar, M E Ae, and N M Anandhan. Analysis and design of noncontact charger using lc load resonant coupling for electrical vehicle system. pages 42–48, 2015.

[20] D. J. Cichon and W. Wiesbeck. Heinrich Hertz wireless experiments at Karlsruhe in the view of modern communication. *IEE Conference Publication*, (411):1–6, 1995.

[21] John C. Schuder, Jerry H. Gold, and Hugh E. Stephenson. An Inductively Coupled RF System for the Transmission of 1 kW of Power Through the Skin. *IEEE Transactions on Biomedical Engineering*, 18 BME(4):265–273, 1971.

[22] Tianjia Sun, Xiang Xie, and Zhihua Wang. *Wireless Power Transfer for Medical Microsystems*, volume 9781461477. Springer New York, New York, NY, 2013.

[23] Ifana Mahbub, Farhan Quaiyum, Md Sakib Hasan, and Syed Kamrul Islam. Electronic Sensor Interfaces With Wireless Telemetry. *Advances in Bioengineering*, 2015.

[24] Gunde Ziegelberger, Rodney Croft, Maria Feychting, Adèle C. Green, Akimasa Hirata, Guglielmo D'Inzeo, Kari Jokela, Sarah Loughran, Carmela Marino, Sharon Miller, Gunnhild Oftedal, Tsutomu Okuno, Eric van Rongen, Martin Röösli, Zenon Sienkiewicz, John Tattersall, and Soichi Watanabe. Guidelines for limiting exposure to electromagnetic fields (100 kHz to 300 GHz), may 2020.

[25] IEEE. *IEEE Standard for Safety Levels With Respect to Human Exposure to Radio Frequency Electromagnetic Fields, 3 kHz to 300 GHz*, volume 2005. 2006.

[26] Tayfun Akin, Khalil Najafi, and Robert M. Bradley. A wireless implantable multichannel digital neural recording system for a micromachined sieve electrode. *IEEE Journal of Solid-State Circuits*, 33(1):109–118, 1998.

[27] Hongming Lyu, Jigong Wang, Jun Ho La, Jin Mo Chung, and Aydin Babakhani. An Energy-Efficient Wirelessly Powered Millimeter-Scale Neurostimulator Implant Based on Systematic Codesign of an Inductive Loop Antenna and a Custom Rectifier. *IEEE Transactions on Biomedical Circuits and Systems*, PP:1–13, 2018.

[28] Chin Lung Yang, Chung Kai Chang, Shuenn Yuh Lee, Soon Jyh Chang, and Lih Yih Chiou. Efficient four-coil wireless power transfer for deep brain stimulation. *IEEE Transactions on Microwave Theory and Techniques*, 65(7):2496–2507, 2017.

[29] Han Joon Kim, Hiroshi Hirayama, Sanghoek Kim, Ki Jin Han, Rui Zhang, and Ji Woong Choi. Review of Near-Field Wireless Power and Communication for Biomedical Applications. *IEEE Access*, 5:21264–21285, 2017.

[30] Michael Faraday. V. Experimental researches in electricity. *Philosophical Transactions of the Royal Society of London*, 122:125–162, jan 1832.

[31] Gabriele Falciasecca. Marconi's early experiments in wireless telegraphy, 1895. *IEEE Antennas and Propagation Magazine*, 52(6):220–221, 2010.

[32] Oren Z. Gall, Chuizhou Meng, Hansraj Bhamra, Henry Mei, Simon W.M. John, and Pedro P. Irazoqui. A Batteryless Energy Harvesting Storage System for Implantable Medical Devices Demonstrated In Situ. *Circuits, Systems, and Signal Processing*, 38(3):1360–1373, 2019.

[33] Sofia Bakogianni and Stavros Koulouridis. A Dual-Band Implantable Rectenna for Wireless Data and Power Support at Sub-GHz Region. *IEEE Transactions on Antennas and Propagation*, PP(c):1, 2019.

[34] John A Rogers, Roozbeh Ghaffari, and Dae-Hyeong Kim. *Stretchable Bioelectronics for Medical Devices and Systems*. 2016.

[35] Eric Y. Chow, Chin Lung Yang, Yuehui Ouyang, Arthur L. Chlebowski, Pedro P. Irazoqui, and William J. Chappell. Wireless powering and the study of RF propagation through ocular tissue for development of implantable sensors. *IEEE Transactions on Antennas and Propagation*, 59(6 PART 2):2379–2387, 2011.

[36] K. Okabe, I. Akita, S. Yamagiwa, T. Kawano, and M. Ishida. A thin film flexible antenna with CMOS rectifier chip for RF-powered implantable neural interfaces. *2015 Transducers - 2015 18th International Conference on Solid-State Sensors, Actuators and Microsystems, TRANSDUCERS 2015*, pages 1751–1754, 2015.

[37] Xian Huang, Yuhao Liu, Gil Woo Kong, Jung Hun Seo, Yinji Ma, Kyung In Jang, Jonathan A. Fan, Shimin Mao, Qiwen Chen, Daizhen Li, Hank Liu, Chuxuan Wang, Dwipayan Patnaik, Limei Tian, Giovanni A. Salvatore, Xue Feng, Zhenqiang Ma, Yonggang Huang, and John A. Rogers. Epidermal radio frequency electronics for wireless power transfer. *Microsystems and Nanoengineering*, 2(June):1–9, 2016.

[38] Simiao Niu, Naoji Matsuhisa, Levent Beker, Jinxing Li, Sihong Wang, Jiechen Wang, Yuanwen Jiang, Xuzhou Yan, Youngjun Yun, William Burnett, Ada S. Y. Poon, Jeffery B.-H. Tok, Xiaodong Chen, and Zhenan Bao. A wireless body area sensor network based on stretchable passive tags. *Nature Electronics*, 2(8):361–368, aug 2019.

[39] Muyang Lin, Nathaniel Georg Gutierrez, and Sheng Xu. Soft sensors form a network. *Nature Electronics*, 2(8):327–328, 2019.

[40] Gerard J Hayes, Ju-hee So, Amit Qusba, Michael D Dickey, and Gianluca Lazzi. Flexible Liquid Metal Alloy (EGaIn) Microstrip Patch Antenna. 60(5):2151–2156, 2012.

[41] Zhaoqian Xie, Raudel Avila, Yonggang Huang, and John A. Rogers. Flexible and Stretchable Antennas for Biointegrated Electronics. *Advanced Materials*, 1902767:1–16, 2019.

[42] Dae Hyeong Kim, Jong Hyun Ahn, Mook Choi Won, Hoon Sik Kim, Tae Ho Kim, Jizhou Song, Yonggang Y. Huang, Zhuangjian Liu, Chun Lu, and John A. Rogers. Stretchable and foldable silicon integrated circuits. *Science*, 320(5875):507–511, 2008.

[43] Yi Fan, Xiongying Liu, Jiming Li, and Tianhai Chang. A miniaturized circularly-polarized antenna for in-body wireless communications. *Micromachines*, 10(1), 2019.

[44] Mahmoud Tavakoli, Mohammad H Malakooti, Hugo Paisana, Yunsik Ohm, Daniel Green Marques, Pedro Alhais Lopes, Ana P Piedade, Anibal T De Almeida, and Carmel Majidi. EGaIn-Assisted Room-Temperature Sintering of Silver Nanoparticles for Stretchable , Inkjet-Printed , Thin-Film Electronics. 1801852:1–7, 2018.

[45] Daniel Green Marques, Pedro Alhais Lopes, Anibal T De Almeida, Carmel Majidi, and Mahmoud Tavakoli. Lab on a Chip stretchable circuits and microelectronics †. 2019.

[46] W. A. Serdijn, A. L.R. Mansano, and M. Stoopman. *Introduction to RF Energy Harvesting*. Elsevier Inc., 2014.

[47] Francesco Giuseppe, Della Corte, Massimo Merenda, Gennaro Giovanni Bellizzi, and T Isernia. Temperature Effects on the Efficiency of Dickson Charge Pumps for Radio Frequency Energy Harvesting. (November), 2018.

[48] Constantine A. Balanis. *Antenna Theory: Analysis and Design, 4th Edition - Constantine A. Balanis*. 2016.

[49] Antenna Theory. Antenna theory vswr defenition, 2009.

[50] Markimicrowave. Return Loss to VSWR Conversion Table.

[51] Kush Agarwal, Yong Xin Guo, and Budiman Salam. Wearable AMC Backed Near-Endfire Antenna for On-Body Communications on Latex Substrate. *IEEE Transactions on Components, Packaging and Manufacturing Technology*, 6(3):346–358, 2016.

[52] J Paleček, M. Vestenický, P Vestenický, and J Spalek. Frequency dependence examination of PCB material FR4 relative permittivity. In *IFAC Proceedings Volumes (IFAC-PapersOnline)*, volume 46, pages 90–94, 2013.

[53] Arno Thielens, Carol Baumbauer, Matthew G. Anderson, Jonathan Ting, Ana C. Arias, and Jan M. Rabaey. Feasability of On-Body Backscattering in the UHF-RFID Band using Screen-Printed Dipole Antennas. In *2019 13th International Symposium on Medical Information and Communication Technology (ISMICT)*, volume 2019-May, pages 1–5. IEEE, may 2019.

[54] Arno Thielens, Igal Deckman, Reza Aminzadeh, Ana C. Arias, and Jan M. Rabaey. Fabrication and Characterization of Flexible Spray-Coated Antennas. *IEEE Access*, 6:62050–62061, 2018.

[55] G. A. Casula, A. Michel, P. Nepa, G. Montisci, and G. Mazzarella. Robustness of Wearable UHF-Band PIFAs to Human-Body Proximity. *IEEE Transactions on Antennas and Propagation*, 64(5):2050–2055, 2016.

[56] G. A. Casula. A Design Rule to Reduce the Human Body Effect on Antennas for Short Range NF-UHF RFID Systems. *2018 2nd URSI Atlantic Radio Science Meeting, AT-RASC 2018*, pages 1–4, 2018.

[57] Giovanni Andrea Casula and Giorgio Montisci. A design rule to reduce the human body effect on wearable pifa antennas. *Electronics (Switzerland)*, 8(2), 2019.

[58] Manikonda Venkateswara Rao, Boddapati Taraka Phani Madhav, Tirunagari Anilkumar, and Badugu Prudhvinadh. Circularly polarized flexible antenna on liquid crystal polymer substrate material with metamaterial loading. *Microwave and Optical Technology Letters*, 62(2):866–874, 2020.

[59] Gurminder Singha, Ashish Singla, and Gurvinder Singh Virk. Modeling and Simulation of a Passive Lower- Body Mechanism for Rehabilitation Modeling and Simulation of a Passive Lower-body Mechanism for Rehabilitation. *Communication, Medicine and Ethics conference (COMET) 2016*, (January), 2016.

Appendices

Appendix A

Python code to configure the RFID Reader

```
#!/usr/bin/env python3
from __future__ import print_function
import time
from time import perf_counter
from datetime import datetime
import mercury
reader = mercury.Reader("tmr:///com4", baudrate=115200)

reader.set_region("open")
print("Original Hop Table:")
print(reader.get_hop_table());
print("\n Reader Hop time: "+str(reader.get_hop_time())+"ms");
reader.set_hop_table([915000,916000])
print("\n New Hop Table:")
print(reader.get_hop_table());
reader.set_read_plan([1], "GEN2", read_power=2700)
time_start = perf_counter()
on_flag = 1

try:
  print("\nStarted")
  reader.start_reading(lambda tag: print(tag.epc),on_time=1000,
   off_time=0)
  while on_flag == 1:
```

```
24      time_now = perf_counter()
25
26      if time_now-time_start > 1000 :
27        print("Set Time Elapsed...")
28        reader.stop_reading()
29        break
30    print("\n Quit")
31  except(KeyboardInterrupt, SystemExit):
32    print("\n Cleaning up...");
33    reader.stop_reading()
```

Listing A.1: Python code to configure the RFID module to read continually.

Appendix B

RF Harvester fabrication

B.1 RF Harvester Circuit Schematics

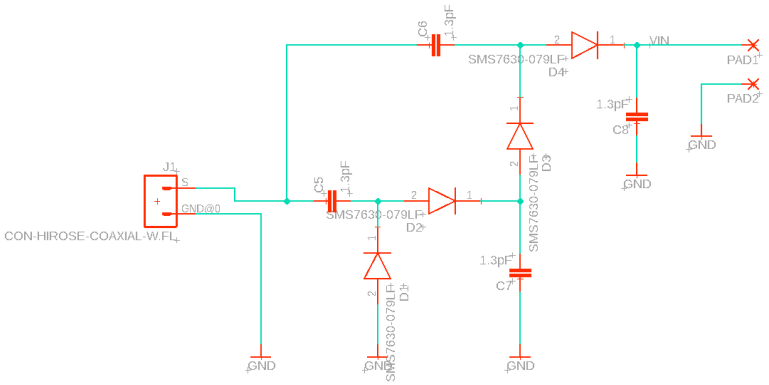

Figure B.1: Schematic of the RF Input and rectification stage of the fabricated RF harvester.

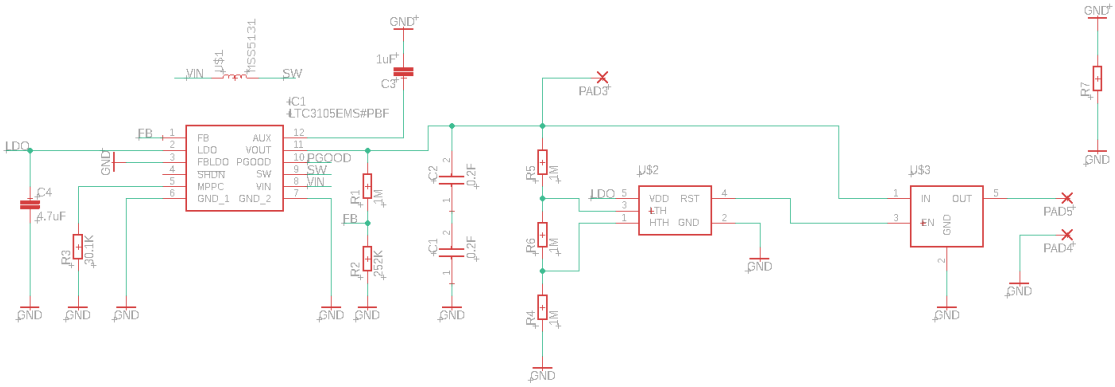

Figure B.2: Schematic of the voltage boost stage of the fabricated RF harvester.

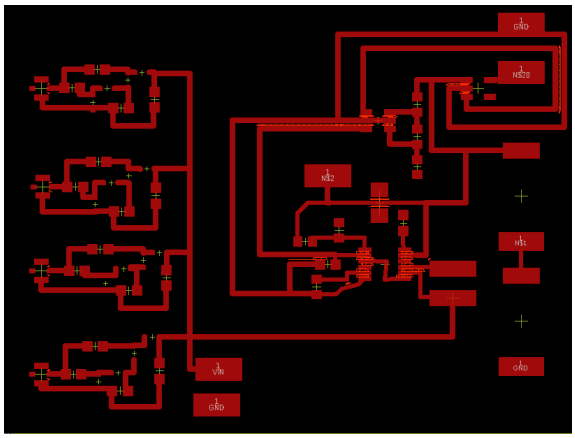

Figure B.3: PCB Top Layer of the fabricated RF harvester.

B.2 RF Harvester Circuit Fabrication

The layout of the RF harvester circuit in Figure B.3 was patterned over a presensitized photo resist 1.6mm PCB (M.G.Chemicals 600 Series - Positive Presensitized Copper Clad Boards) using laser ablation to remove the photo-resistive layer and expose the copper laminate(Figure B.4). Then it was chemically etched using peroxydisulfuric acid($Na_2S_2O_8$) to remove the exposed cooper(Figure B.5). Afterwards the sheet is rinsed with acetone to remove the remaining photo-resistive layer, resulting in the PCB shown in Figure 3.11.

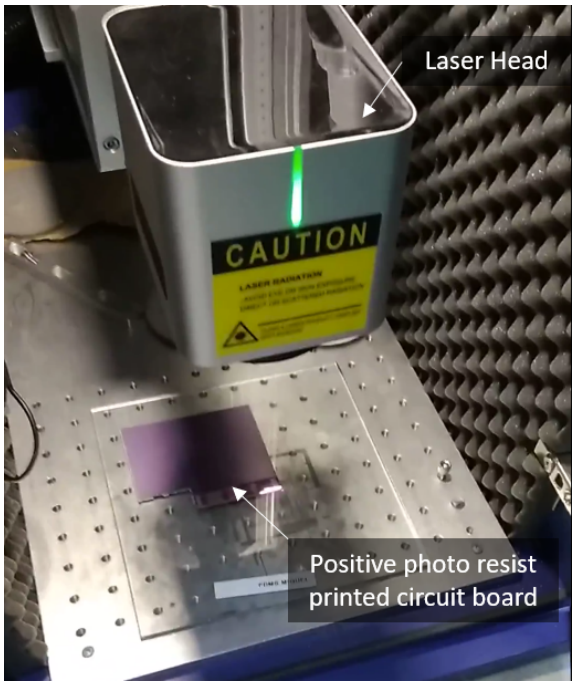

Figure B.4: Picture of the laser ablation process.

Figure B.5: Picture of the chemical etching process.